Supporting Information for

Catalytic Iron-Carbene Intermediate Revealed in a Cytochrome *c* Carbene Transferase

Russell D. Lewis[a,1], Marc Garcia-Borràs[b,1], Matthew J. Chalkley[c], Andrew R. Buller[c,d], K. N. Houk[b,2], S. B. Jennifer Kan[c,2], Frances H. Arnold[a,c,2]

[a] Division of Biology and Bioengineering, California Institute of Technology, Pasadena, CA, 91125, USA.
[b] Department of Chemistry and Biochemistry, University of California Los Angeles, Los Angeles, CA, 90095, USA.
[c] Division of Chemistry and Chemical Engineering, California Institute of Technology, Pasadena, CA, 91125, USA.
[d] Current address: Department of Chemistry, University of Wisconsin-Madison, Madison, WI, 53706, USA

[1] Denotes equal author contribution.
[2] To whom correspondence should be addressed: houk@chem.ucla.edu, sbjkan@caltech.edu, frances@cheme.caltech.edu

www.pnas.org/cgi/doi/10.1073/pnas.1807027115

I. Materials and Methods

Unless otherwise noted, all chemicals and reagents for chemical reactions were obtained from commercial suppliers (Acros, Arch Bioscience, Fisher Scientific, Sigma-Aldrich, TCI America, VWR) and used without further purification. Multitron shakers (Infors, Annapolis Junction, MD) were used for cell growth. UV-Vis spectroscopy was performed using a Shimadzu UV-1800 spectrophotometer (Shimadzu, Carlsbad, CA). Sonication was performed using a Qsonica Q500 sonicator. Silica gel chromatography purifications were carried out using AMD Silica Gel 60, 230-400 mesh. ^{1}H NMR spectra were recorded on a Bruker Prodigy 400 MHz instrument and are internally referenced to the residual solvent peak (chloroform). Data for ^{1}H NMR are reported in the conventional form: chemical shift (δ ppm), multiplicity (s = singlet, d = doublet, t = triplet, q = quartet, hept = heptet, m = multiplet, br = broad, app = appears as), coupling constant (Hz), integration. Gas chromatography (GC) analyses were carried out using a Shimadzu GC-17A gas chromatograph, a flame ionization detector (FID), and J&W HP-5 (30 m x 0.32 mm, 0.25 µm film; 90 °C hold 1 min, 90 to 110 °C at 15 °C/min, 110 to 280 °C at 60 °C/min, 280 °C hold 1 min, 6.2 min total). Analytical chiral high pressure liquid chromatography (HPLC) was performed with a HP-Agilent 1100 series instrument using *i*-PrOH and hexanes as the mobile phase, with visualization at 210 nm. A Chiralcel OD-H column was used for chiral separations (4.6 mm x 25 cm).

Plasmid pET22 was used as a cloning vector, and cloning was performed using Gibson assembly (1). The cytochrome *c* maturation plasmid pEC86 (2) was used as part of a two-plasmid system to express prokaryotic cytochrome *c* proteins. Cells were grown using Lysogeny Broth medium or HyperBroth (AthenaES, Baltimore, MD) with 100 µg/mL ampicillin and 20 µg/mL chloramphenicol ($LB_{amp/chlor}$ or $HB_{amp/chlor}$). Primer sequences are available upon request. Electrocompetent *Escherichia coli* cells were prepared following the protocol of Sambrook *et al.* (3). T5 exonuclease, Phusion polymerase, and *Taq* ligase were purchased from New England Biolabs (NEB, Ipswich, MA). Sodium phosphate (NaPi, 20 mM, pH 7.5) was used as a buffering system for purified proteins, unless otherwise specified. M9-N minimal medium (abbreviated as M9-N buffer; pH 7.4) was used without a carbon source; it contains 47.7 mM Na_2HPO_4, 22.0 mM KH_2PO4, 8.6 mM NaCl, 2.0 mM $MgSO_4$, and 0.1 mM $CaCl_2$.

II. General Procedures

(A) Plasmid construction.

All variants described in this paper were cloned and expressed using the pET22(b)+ vector (MilliporeSigma, St. Louis, MO). The gene encoding *Rhodothermus marinus* cyt *c* V75T M100D M103E (*Rma* TDE) was obtained as a single gBlock (Integrated DNA Technologies, Coralville, IA) (4), codon-optimized for *E. coli*, and cloned using Gibson assembly (1) into pET22(b)+ between restriction sites *Nde*I and *Xho*I in frame. The gene encoding *Rma* TDE contained an *N*-terminal pelB leader sequence and 6xHisTag (MKYLLPTAAAGLLLLAAQPAMAHHHHHH) and had the first seven amino acids of mature, wild-type *Rma* cyt *c* removed (TESGTAA). This plasmid was co-transformed with the cytochrome *c* maturation plasmid pEC86 (2) into *E. cloni*® EXPRESS BL21(DE3) cells (Lucigen, Middleton, WI).

DNA coding sequence of *Rma* cyt *c* V75T M100D M103E with an *N*-terminal pelB leader sequence and 6xHisTag

ATGAAATACCTGCTGCCGACCGCTGCTGCTGGTCTGCTGCTCCTCGCTGCCCAGCCGGCG
ATGGCCCATCATCATCATCACCACCAAGACCCGGAAGCACTGGCAGCGGAAATTGGTCCG
GTCAAACAGGTGAGCCTGGGTGAACAGATTGATGCGGCCCTGGCGCAACAGGGAGAACA
GCTCTTCAACACGTATTGTACTGCGTGCCACCGTCTGGATGAGCGTTTTATCGGACCGGCC
CTGCGCGATGTTACCAAACGTCGTGGGCCGGTTTACATCATGAACACGATGCTGAACCCG
AATGGGATGATCCAGCGTCATCCGGTGATGAAACAGCTCGTGCAGGAATATGGGACCATG
GATACCGATGAGGCCCTGAGTGAAGAACAAGCGCGCGCAATTCTGGAGTATCTGCGCCAG
GTTGCGGAAAACCAGTAATGA

Amino acid sequence of *Rma* cyt *c* V75T M100D M103E with an *N*-terminal pelB leader sequence and 6xHisTag

MKYLLPTAAAGLLLLAAQPAMAHHHHHHQDPEALAAEIGPVKQVSLGEQIDAALAQQGEQLFN
TYCTACHRLDERFIGPALRDVTKRRGPVYIMNTMLNPNGMIQRHPVMKQLVQEYGTMDTDEAL
SEEQARAILEYLRQVAENQ

(B) Cytochrome *c* expression and purification.

Purified cytochrome *c* proteins were prepared as follows. In a 4 L flask, one liter HyperBroth (AthenaES) containing 100 µg/mL ampicillin and 20 µg/mL chloramphenicol ($HB_{amp/chlor}$) was inoculated with an overnight culture (20 mL, Lysogeny Broth, with 100 µg/mL ampicillin, 20 µg/mL chloramphenicol, $LB_{amp/chlor}$) of recombinant *E. cloni*® EXPRESS BL21(DE3) cells containing a pET22(b)+ plasmid encoding the cytochrome *c* variant, and the pEC86 plasmid. The culture was shaken at 37°C and 200 rpm (no humidity control) until the OD_{600} was 0.7 (approximately 3 hours). The culture was placed on ice for 30 minutes, and isopropyl β-D-1-thiogalactopyranoside (IPTG) and 5-aminolevulinic acid (ALA) were added to final concentrations of 20 µM and 200 µM, respectively.

The incubator temperature was reduced to 25°C, and the culture was allowed to shake for 20 hours at 200 rpm. Cells were harvested by centrifugation (4 °C, 15 min, 4,000xg), and the cell pellet was stored at −20°C until further use (at least 24 hours). The cell pellet was resuspended in buffer containing 100 mM NaCl, 20 mM imidazole, and 20 mM Tris-HCl buffer (pH 7.5 at 25 °C) and cells were lysed by sonication (4 minutes, 1 second on, 1 second off, 30% duty cycle; Qsonica Q500 sonicator). Cell lysate was placed in a 75 °C heat bath for 10 minutes, and cell debris was removed by centrifugation for 20 min (30,000xg, 4 °C). Supernatant was sterile filtered through a 0.45 µm cellulose acetate filter and purified using a 1 mL Ni-NTA column (HisTrap HP, GE Healthcare, Piscataway, NJ) using an AKTA purifier FPLC system (GE Healthcare). The cytochrome *c* protein was eluted from the column by running a gradient from 20 to 500 mM imidazole over 10 column volumes.

The purity of the collected cytochrome *c* fractions was analyzed using sodium dodecyl sulfate-polyacrylamide gel electrophoresis (SDS-PAGE). Pure fractions were pooled and concentrated using a 3 kDa molecular weight cut-off centrifugal filter. Protein for crystallography was dialyzed overnight into 20 mM Tris-HCl buffer (pH 7.5 at 25 °C) using 3.5 kDa molecular weight cut-off dialysis tubing. Protein for non-crystallography use was dialyzed overnight into 20 mM sodium phosphate buffer (pH 7.5) using 3.5 kDa molecular weight cut-off dialysis tubing. The dialyzed protein was further concentrated using a 3 kDa molecular weight cut-off centrifugal filter, flash-frozen on dry ice, and stored at −20°C.

The concentration of cytochrome *c* was determined in triplicate using the hemochrome assay described in section (D).

(C) ^{57}Fe-labelled cytochrome *c* expression and purification.

In order to prepare protein samples for Mössbauer spectroscopy, ^{57}Fe-labelled *Rma* cyt *c* was expressed and purified, using a protocol adapted from Liptak *et al* (5).

For 1 L ^{57}Fe media:

950 mL	basic salts buffer
10 mL	trace metals mix
10 mL	vitamin cocktail
300 µL	^{57}Fe / H_2SO_4 solution
10 mL	1 M $MgCl_2$
5 g	L/D-glucose
1 g	NH_4Cl
16.8 mg	5-aminolevulinic acid (ALA)
30 mg	thiamine hydrochloride
1 mL	20 mg/mL chloramphenicol in ethanol
1 mL	100 mg/mL ampicillin in water

For 950 mL basic salts buffer:

- 950 mL water
- 13.0 g KH_2PO_4
- 13.1 g $K_2HPO_4 \cdot (3H_2O)$
- 17.1 g $Na_2HPO_4 \cdot (7H_2O)$
- 3.6 g Na_2SO_4

Adjusted pH to 7.4 with 5M NaOH, autoclaved, and stored at room temperature.

For 100 mL Trace metals mix:

- 90 mL water
- 600 mg calcium chloride, dihydrate
- 120 mg manganese chloride, tetrahydrate
- 80 mg cobalt chloride, hexahydrate
- 70 mg zinc sulfate, heptahydrate
- 30 mg copper chloride, dihydrate
- 2 mg boric acid
- 500 mg EDTA

Adjusted pH to 7.4 with 5M NaOH, and added water until final volume was 100 mL. Solution was deep purple. The solution was sterile filtered through a 0.2 µm PES membrane and stored at –20°C.

For 100 mL vitamin cocktail:

- 100 mL water
- 10 mg biotin
- 10 mg choline chloride

- 10 mg folic acid
- 10 mg nicotinamide
- 10 mg calcium D-pantothenate
- 10 mg pyridoxal phosphate
- 1 mg riboflavin

The solution was sterile filtered through a 0.2 µm PES membrane, and stored at –20°C.

For 600 µL ^{57}Fe / H_2SO_4 solution:

- 25.0 mg ^{57}Fe (95% enrichment, Isoflex USA, San Francisco)
- 600 µL 2 M H_2SO_4

H_2SO_4 was added to the iron powder under anaerobic conditions, and allowed to shake overnight, until the iron was dissolved. The solution was pale blue, and was stored at room temperature under anaerobic conditions.

Purified ^{57}Fe cytochrome *c* proteins were prepared as follows. In a 125 mL flask, 30 mL of $HB_{amp/chlor}$ was inoculated with an overnight culture (1 mL, $LB_{amp/chlor}$) of recombinant *E. cloni*® EXPRESS BL21(DE3) cells containing a pET22(b)+ plasmid encoding the cytochrome *c* variant, and the pEC86 plasmid. The culture was shaken at 37°C and 200 rpm (no humidity control) until the OD_{600} was 0.7 (approximately 3 hours). In a 4 L flask, one liter of ^{57}Fe medium was inoculated with 20 mL of the late-log phase $HB_{amp/chlor}$ culture. The culture was again shaken at 37°C and 200 rpm (no humidity control) until the OD_{600} was 0.3 (approximately 4 more hours). The culture was placed on ice for 30 minutes, and isopropyl β-D-1-thiogalactopyranoside (IPTG) and 5-aminolevulinic acid (ALA) were added to final concentrations of 20 µM and 200 µM, respectively.

After addition of IPTG and ALA, the culture was returned to the shaker, allowed to shake for 24 hours at 37 °C, 200 rpm. Cells were harvested and lysed using the same procedure as described in (B). ^{57}Fe-labelled protein was then purified as described in (B).

(D) Hemochrome assay.

A solution of sodium dithionite (10 mg/mL) was prepared in M9-N buffer. Separately, a solution of 1 M NaOH (0.4 mL) was mixed with pyridine (1 mL), followed by centrifugation (10,000xg, 30 seconds) to separate the excess aqueous layer gave a pyridine-NaOH solution. To a cuvette containing 10 µL purified protein solution and 690 µL M9-N buffer, 50 µL of dithionite solution and 250 µL pyridine-NaOH solution were added. The cuvette was sealed with Parafilm, and the UV-Vis spectrum was recorded immediately. Cytochrome *c* concentration was determined using $\varepsilon_{550-535} = 22.1\ mM^{-1}cm^{-1}$ (4,6).

(E) Synthesis and characterization of authentic organosilicon product

Ethyl 2-(dimethylphenylsilyl)propanoate was prepared in a similar manner to that published in Kan et al. 2016 (4). In a 25 mL round bottom flask, 0.281 g of dimethylphenylsilane (2.0 mmol, 2.0 equiv.) were added, followed by, $Rh_2(OAc)_4$ (1.1 mg, 0.25 mol%) and 5 mL of dichloromethane. The mixture was cooled to 0°C, after which 0.128 g of ethyl-2-diazopropanoate (1.0 mmol, 1.0 equiv.) was added dropwise to the solution. The reaction was allowed to slowly warm up to room temperature over 4 hours and stirred at room temperature for another 1 hour. Evaporation of the organic solvent and purification by silica column chromatography using EtOAc and hexane as eluents afforded the organosilicon product ethyl 2-(dimethylphenylsilyl)propanoate with 54% yield. ^{1}H NMR was used to confirm product identity and purity.

(F) Biocatalytic reactions

In an anaerobic chamber, 10 µL of 80 µM purified protein was added to 350 µL of 20 mM sodium phosphate buffer (NaPi, pH 7.5) in a 2 mL crimp vial. Next, the protein was reduced by adding 20 µL $Na_2S_2O_4$ (200 mM in NaPi, pH 7.5), and the reaction was initiated with the addition of reactants, 10 µL $PhMe_2SiH$ (400 mM in acetonitrile) and 10 µL Me-EDA (400 mM in MeCN). The vial was crimp sealed, removed from the anaerobic chamber, and shaken at 400 rpm at room temperature for 2 hours. At the end of the reaction, the crimp vial was opened and the reaction was quenched with cyclohexane (1 mL). Internal standard was added (20 µL of 1,2,3-trimethoxybenzene in toluene) and the reaction mixture was transferred to a microcentrifuge tube, vortexed (1 minute), then centrifuged (14,000xg, 5 min) to completely separate the organic and aqueous layers. The organic layer (750 µL) was removed for GC and chiral HPLC analysis. All biocatalytic reactions were performed in triplicate. The total turnover numbers (TTNs) reported are calculated with respect to the protein catalyst and represent the total number of turnovers obtained using the catalyst under the stated reaction conditions.

Concentration of organosilicon product was calculated based on the ratio of areas between the product peak and internal standard peak, as measured by GC-FID.

Stock solutions of chemically synthesized ethyl 2-(dimethylphenylsilyl)propanoate were prepared at various concentrations (20 to 200 mM in MeCN). To a microcentrifuge tube were added 360 µL 20 mM sodium phosphate buffer, 20 µL $Na_2S_2O_4$ (200 mM in NaPi, pH 7.5), 20 µL organosilicon product, 20 µL internal standard (20 mM 1,2,3-trimethoxybenzene in toluene) and 1 mL cyclohexane. The mixture was vortexed (1 minute) then centrifuged (14,000xg, 5 min) to completely separate the organic and aqueous layers. The organic layer (750 µL) was removed for GC analysis. Each concentration was prepared in duplicate, and both data points are shown for each concentration (Figure S11). The standard curves plot product concentration in mM (x-axis) against the ratio of product area to internal standard area on the GC (y-axis).

Enantiomeric excess for biocatalytically synthesized products was determined using chiral HPLC, with a Chiralcel OD-H column as the stationary phase and 1% isopropanol, 99% hexanes as the mobile phase, at 40ºC for 30 minutes.

(G) UV-Visible spectroscopy

UV-Visible spectra were collected at room temperature between 600 and 380 nm on a UV-1800 Shimadzu spectrophotometer in quartz cuvettes sealed with Parafilm (aerobic conditions) or a screw cap with a pierceable septum (anaerobic conditions). Sodium phosphate (NaPi, 20 mM, pH 7.5) was used as a buffer system. Spectra of reduced *Rma* TDE was taken in buffer supplemented with 50 mM sodium dithionite to ensure complete reduction of the ferrous iron, and various co-solvents were added to demonstrate that the spectral characteristics are similar in 1% isopropanol, 5% acetonitrile, and 15% dimethylsulfoxide. Spectra of reduced, Me-EDA-treated *Rma* TDE was taken in buffer containing 50 mM sodium dithionite, 10 mM ethyl 2-diazo propanoate, and 1% isopropanol. Co-solvents were added to demonstrate that the addition of 5% acetonitrile or 15% dimethylsulfoxide did not substantially impact the spectrum. For spectra taken under anaerobic conditions, the headspace of the cuvettes was de-gassed with argon for 5 minutes prior to the addition of sodium dithionite and Me-EDA.

(H) X-ray crystallography

Fine screening for *Rma* TDE crystallization was performed around crystallography conditions previously reported to yield crystals of wild-type *Rma* cyt *c* (7). Crystals were grown against a 1-mL reservoir with mother liquor comprised of 2.0 µL of 14.0 mg/mL *Rma* TDE (in 20 mM Tris HCl, pH 7.5) and 1.0 µL of well solution. Very small crystals were observed after two weeks in 1.8-1.9 M $(NH_4)_2SO_4$, 2% isopropanol. Further optimization failed to yield larger crystals, but showed that the protein crystallized within the range of 1.4-1.9 M $(NH_4)_2SO_4$, 1-3% isopropanol. Additive screening was performed using an additive screening kit (Hampton Research, Aliso Viejo, CA) and with mother liquor comprised of 2.0 µL of 14.0 mg/mL *Rma* TDE, 1.0 µL of well solution (1.7 M $(NH_4)_2SO_4$, 1.5% isopropanol), and 0.2 µL of additive solution. Additive screening showed that addition of NaSCN yielded larger and more numerous crystals. Further fine screening around this condition revealed that the best crystals were obtained using 1.43-1.48 M $(NH_4)_2SO_4$, 300-400 mM NaSCN, and 1.5% isopropanol (2.0 µL of 14.0 mg/mL *Rma* TDE, 1.0 µL well solution). Under these conditions, crystals formed over 3-5 days, and reached maximum size after 7-10 days. Crystals were cryo-protected by addition of ethylene glycol to the well solution to a final concentration of 20%. Crystals were flash frozen and stored in liquid N_2 until diffraction.

For crystals soaked with the carbene precursor Me-EDA, the mother liquor was supplemented with 1 M Me-EDA in isopropanol to a final concentration of 40 mM Me-EDA. Crystals were soaked at room temperature for 30 minutes before moving the samples to 4ºC. At 4ºC, the crystals were soaked for approximately 1 minute in a solution of mother liquor supplemented with 40 mM Me-EDA and 50 mM sodium dithionite before flash-freezing in liquid nitrogen. Prolonged soaking in either of the Me-EDA supplemented solutions caused the crystals to dissolve.

Diffraction data were collected remotely at the Stanford Synchrotron Radiation Laboratories on beamline 12-2, with a wavelength of 0.97946 Å, and at a temperature of 100 K. Crystals routinely diffracted at or below 1.7 Å, and the data were integrated and scaled using XDS (8) and AIMLESS (9). A resolution cutoff of $I/\sigma > 2.5$ was applied along all axes of diffraction. These data contributed to model quality as judged by R_{free} in the final bin < 0.27. The structure was solved using molecular replacement with PHASER (10), as implemented in CCP4 (11). For *Rma* TDE, the search model comprised a single monomer of wild-type *Rma* cyt *c* (PDB ID: 3CP5) (12) subjected to 10 cycles of geometric idealization in Refmac5 (13) and removal of all ligands. For carbene-bound *Rma* TDE, the search model comprised a single monomer of *Rma* TDE (PDB ID: 6CUK) subjected to 10 cycles of geometric idealization in Refmac5 and removal of all ligands. Model building was performed in Coot (14) beginning with data processed at 2.2 Å, followed by subsequent inclusion of increasingly higher resolution shells of data with relaxed geometric constraints. Refinement was performed using Refmac5. The MolProbity server (15) was used to identify rotamer flips and clashes. After the protein, ligand, and solvent atoms were built, TLS operators were added to refinement (16), which resulted in substantial improvements in R_{free} for the models. Crystallographic and refinement statistics are reported in Table S1. The carbene ligand was modelled in a single conformation at 100% occupancy, which resulted in the atoms comprising the Fe–C bond to have B-factors of 14.74 and 21.36, respectively. Occupancy was not refined by B-factor matching, as the electron density suggested only a single conformation, and B-factors on both atoms were both sufficiently low and similar to indicate high occupancy in the crystal. The carbene-bound *Rma* TDE structure is deposited with PDB ID: 6CUN, and the *Rma* TDE structure without the carbene ligand is deposited with PDB ID: 6CUK. Analysis of the protein structures with MolProbity showed that the carbene-bound *Rma* TDE structure had a MolProbity score of 1.0, and the *Rma* TDE structure had a MolProbity score of 0.9, putting both structures in the highest percentile rank for MolProbity scores. The carbene-bound *Rma* TDE structure contains

98.15% Ramachandran-favored rotamers, with no Ramachandran outliers, and the *Rma* TDE structure contains 99.12% Ramachandran-favored rotamers and no Ramachandran outliers.

(I) Mössbauer spectroscopy

General Description of Mössbauer Spectroscopy:
Mössbauer spectra were recorded on a spectrometer from SEE Co. (Edina, MN) operating in the constant acceleration mode in a transmission geometry. The sample was kept in an SVT-400 cryostat form Janis (Wilmington, MA). The quoted isomer shifts are relative to the centroid of the spectrum of a metallic foil of α-Fe at room temperature (RT). Solution samples were transferred to a sample cup and chilled to 77 K inside of the glovebox, and unless noted otherwise, quickly removed from the glovebox and immersed in liquid N_2 until mounted in the cryostat. Data analysis was performed using version 4 of the program WMOSS (www.wmoss.org) and quadrupole doublets were fit to Lorentzian lineshapes except where noted. See discussion below for detailed notes on the fitting procedure.

Sample preparation for Mössbauer Spectroscopy:
Sample preparation conditions for Mössbauer samples were designed to be similar to those conditions used to assay the biocatalytic activity of *Rma* TDE, as shown in Supplementary Figure 4F.

In an anaerobic chamber, an aliquot of ^{57}Fe-labelled purified *Rma* TDE (4.00 mM) was thawed. For the reduced *Rma* TDE sample, 341 µL of protein (4.00 mM in 20 mM NaPi, pH 7.5) was added to a Mössbauer cup containing 3.7 mg sodium dithionite. Acetonitrile (18 µL) was added to the Mössbauer cup, and the sample was pipetted up and down to ensure the sample was homogenous (approximately 10 seconds). The sample was then flash-frozen on liquid nitrogen. Final concentrations: 3.8 mM protein, 19 mM NaPi (pH 7.5), 50 mM sodium dithionite, 5% acetonitrile.

For the reduced Me-EDA-treated *Rma* TDE sample, 341 µL of protein (4.0 mM in 20 mM NaPi, pH 7.5) was added to a Mössbauer cup containing 3.7 mg sodium dithionite. 18 µL of 1.0 M Me-EDA in acetonitrile was added to the Mössbauer cup, and the sample was pipetted up and down to ensure the sample was homogenous (approximately 10 seconds). The sample was then flash-frozen on liquid nitrogen. Final concentrations: 3.8 mM protein, 19mM NaPi (pH 7.5), 50 mM sodium dithionite, 50 mM Me-EDA, 5% acetonitrile.

(J) Electron paramagnetic resonance (EPR) spectroscopy

General Description of EPR Spectroscopy:
EPR spectra were recorded on a Bruker EMX X-band CW-EPR Spectrometer (Bruker, Billerica, MA) at 4 K. using Bruker Win-EPR software (ver. 3.0). Data were collected with in parallel mode with a power of 10 mW, and in perpendicular mode with a power of 2 mW.

Sample preparation for EPR spectroscopy:
In an anaerobic chamber, an aliquot of purified *Rma* TDE was thawed and diluted to 1.00 mM with 20 mM NaPi, pH 7.5 with 10% v/v DMSO. Solid sodium dithionite was added to the purified

Rma TDE. For the reduced *Rma* TDE sample, 250 µL of the reduced protein (1.00 mM in 20 mM NaPi, pH 7.5) was added to an EPR tube containing 13 µL DMSO, vortexed briefly, and flash-frozen on liquid nitrogen. Final concentrations: 950 µM protein, 30 mM sodium dithionite, 19 mM NaPi, 15% v/v DMSO. For the reduced, Me-EDA treated *Rma* TDE sample, 250 µL of reduced protein was added to an EPR tube containing 13 µL 1M Me-EDA in DMSO, vortexed briefly, and flash-frozen on liquid nitrogen. Final concentrations: 950 µM protein, 50 mM Me-EDA, 30 mM sodium dithionite, 19 mM NaPi, 15% v/v DMSO. Empty cavity measurements were performed without putting an EPR tube into the machine.

(K) Quantum Mechanics (Density Functional Theory) calculations

Density Functional Theory (DFT) calculations were carried out using Gaussian09 (17). A truncated model containing the porphyrin pyrrole core, Fe center and an imidazole to mimic histidine as Fe-axial ligand was used. Geometry optimizations and frequency calculations were performed using (U)B3LYP (18,19,20) functional with the SDD basis set for iron and 6-31G(d) on all other atoms. Transition states had one negative force constant corresponding to the desired transformation. All stationary points were verified as minima or first-order saddle points by a vibrational frequency analysis. Intrinsic reaction coordinate (IRC) calculations were performed to ensure that the optimized transition states connect the corresponding desired reactants and products. Enthalpies and entropies were calculated for 1 atm and 298.15 K. A correction to the harmonic oscillator approximation, as discussed by Truhlar and co-workers, was also applied to the entropy calculations by raising all frequencies below 100 cm^{-1} to 100 cm^{-1} (21,22) using Goodvibes v.1.0.1 python script (23). Single point energy calculations were performed using the dispersion-corrected functional (U)B3LYP-D3(BJ) (24,25) with the Def2TZVP basis set on all atoms, and within the CPCM polarizable conductor model (diethyl ether, $\varepsilon = 4$) (26,27) to have an estimation of the dielectric permittivity in the enzyme active site. The use of a dielectric constant $\varepsilon=4$ has been proved to be a good and general model to account for electronic polarization and small backbone fluctuations in enzyme active sites (28,29). All energy values discussed in the manuscript correspond to the quasi-harmonic corrected Gibbs energies (ΔG-qh) at (U)B3LYP-D3(BJ)/Def2TZVP/PCM(diethyl ether)//(U)B3LYP/6-31G(d)+SDD(Fe)/PCM(diethyl ether) level, if not otherwise noted.

The methodology employed in this study, based on the use of (U)B3LYP density functional, is very similar to that used by Shaik group for the study of iron carbene porphyrins (30), and more recently by Luis, Solà, Costas and co-workers to study non-heme iron carbene transfer reactions (31). (U)B3LYP has also been extensively proven to accurately perform in the computational modelling of iron-oxo chemistry (32,33,34,35,36).

The modelling of the open-shell electronic state was done by using a Gaussian09 “stable = opt” calculation (37,38,39) to generate a singlet open-shell orbital guess from the triplet optimized geometry, followed by a full optimization of the system starting from this guess. Optimized DFT structures are illustrated with CYLView (40).

(L) Hybrid Quantum Mechanics/Molecular Mechanics (QM/MM) calculations

QM/MM calculations within the ONIOM approach (41,42) were carried out using Gaussian09 (17). Geometry optimizations were performed using (U)B3LYP (18,19,20) functional in combination with the SDD basis set for iron and 6-31G(d) on all other atoms and AmberFF14Sb force field, using the QuadMac algorithm (43) as implemented in Gaussian09 and a mechanical embedding

scheme. Stationary points were verified as minima by a vibrational frequency analysis, and thermal corrections were calculated for 1 atm and 298.15 K. A correction to the harmonic oscillator approximation, as discussed by Truhlar and co-workers, was also applied to the entropy calculations by raising all frequencies below 100 cm^{-1} to 100 cm^{-1} (21,22) using Goodvibes v1.0.1 python script (23). Single point energy calculations were performed at the (U)B3LYP/Def2TZVP:AmberFF14Sb level, and using an electrostatic embedding scheme.
Snapshots for QM/MM calculations were obtained from classical MD trajectories, as described below, and included all the protein residues, cofactors, counterions and water molecules contained in a <3 Å shell around the protein structure. QM region (82 atoms) included the heme porphyrin pyrrole core and carboxylate groups, Fe center and a histidine imidazole ring, the carbene atoms and the bridging water molecule. The total charge of the QM region was -2. In the QM/MM optimizations the active site region to be optimized included all QM atoms and all the residues and water molecules of the MM region within 6 Å from any atom in the QM region. The TAO (Toolkit to Assist ONIOM Calculations) package of scripts by Tao and Schlegel (44) was used to assist the preparation and conversion of the necessary files from Amber and PDB formats to Gaussian09 format.

(M) Computational modelling of Mössbauer spectroscopic parameters

^{57}Fe Mössbauer isomer shifts can be computationally estimated by computing electron density values at the iron nuclear positions (45). Isomer shifts are linearly related to electron density at the Mössbauer absorbing nucleus, as defined by the linear equation (*eq. 1*):

$$\delta_{MB} = \alpha\,(\rho(0) - C) + \beta \qquad\qquad (eq. 1)$$

where α, β and C are fit parameters to be determined by linear regression of experimental isomer shifts and the corresponding DFT computed electron densities at the Fe nuclei. A calibration for diverse DFT functionals and basis sets for a test set of iron-containing complexes comprising a large range of oxidation states and ligand environments was performed by Römelt and Neese (46), which is the one used in our current study.

DFT calculations for Mössbauer isomer shift predictions were done using the ORCA program, version 4.0.1.2 (47). Single point calculations were performed on the corresponding (U)B3LYP optimized model system geometries described above, using the meta-GGA TPSS functional (48) in combination with the TZVP basis set to obtain electron density values at the Fe center. These electron density values were then used to extrapolate the isomer shift values using the corresponding Römelt and Neese calibrations (46). Broken-symmetry solutions for the singlet open-shell electronic configuration were found by first converging to a triplet self-consistent field solutions and then performing spin flip on carbene *C* central atom and converging to broken-symmetry state of $M_S = 0$.

Although quadrupole splitting parameters were also determined for the studied systems, due to the fact that they typically exhibit larger errors than the calculated isomer shifts (49), especially in a protein environment, they have not been used for quantitative analysis in this study.

(N) Molecular Dynamics (MD) simulations

Molecular Dynamics simulations were performed using the GPU code (*pmemd*) (50) of the AMBER 16 package (51). Parameters for the carbene-bound IPC were generated within the *antechamber* and MCPB.py (52) modules in AMBER16 package using the general AMBER force field (*gaff*) (53), with partial charges set to fit the electrostatic potential generated at the B3LYP/6-31G(d) level by the RESP model (54). The charges were calculated according to the Merz–Singh–Kollman scheme (55,56) using the Gaussian 09 package (17). Protonation states of protein residues were predicted using H++ server. Each protein was immersed in a pre-equilibrated truncated cuboid box with a 10 Å buffer of TIP3P (57) water molecules using the *leap* module, resulting in the addition of around 6,400 solvent molecules. The systems were neutralized by addition of explicit counter ions (Na^+ and Cl^-). All subsequent calculations were done using the widely tested Stony Brook modification of the Amber14 force field (*ff14sb*) (58). A two-stage geometry optimization approach was performed. The first stage minimizes the positions of solvent molecules and ions imposing positional restraints on the solute by a harmonic potential with a force constant of 500 $kcal \cdot mol^{-1} \cdot Å^{-2}$. The second stage minimizes all the atoms in the simulation cell except those involved in the harmonic distance restraint. The systems were gently heated using six 50 ps steps, incrementing the temperature by 50 K for each step (0–300 K) under constant-volume and periodic-boundary conditions. Water molecules were treated with the SHAKE algorithm such that the angle between the hydrogen atoms was kept fixed. Long-range electrostatic effects were modelled using the particle-mesh-Ewald method (59). An 8 Å cut-off was applied to Lennard–Jones and electrostatic interactions. Harmonic restraints of 30 $kcal \cdot mol^{-1}$ were applied to the solute and the Andersen equilibration scheme was used to control and equalize the temperature. The time step was kept at 1 fs during the heating stages, allowing potential inhomogeneities to self-adjust. Each system was then equilibrated for 2 ns with a 2 fs time step at a constant volume. Production trajectories were then run for an additional 1000 ns (1 μs) under the same simulation conditions. Trajectories were processed and analyzed using the cpptraj (60) module from Ambertools utilities. Snapshots for QM/MM calculations were obtained from a clusterization analysis of MD trajectories using cpptraj, where a representative snapshot from the most populated cluster was selected.

III. Tables and Figures

Table S1A. Data collection and refinement statistics of *Rma* TDE

	Carbene-bound *Rma* TDE[a] (6CUN)	*Rma* TDE[a] (6CUK)
Data collection		
Space group	$P3_221$	$P3_221$
Cell dimensions		
a, *b*, *c* (Å)	60.3, 60.3, 77.2	60.0, 60.0, 77.3
α, β, γ (°)	90.0, 90.0, 120.0	90.0, 90.0, 120.0
Resolution (Å)	38.62-1.29 (1.32-1.29)[b]	38.65-1.47 (1.50-1.47)[b]
R_{merge}, R_{meas}, R_{pim}	0.070, 0.072, 0.016 (1.2, 1.2, 0.30)	0.067, 0.073, 0.028 (0.425, 0.469, 0.270)
$I/\sigma(I)$	21.4 (2.9)	15.2 (3.7)
$CC_{1/2}$	1.0 (0.95)	1.0 (0.95)
Completeness (%)	100 (100)	99.8 (98.9)
Multiplicity	19.4 (16.6)	6.6 (5.6)
Refinement		
Resolution (Å)	1.29	1.47
No. reflections	39554	27920
R_{work} / R_{free}	0.182 / 0.202	0.183 / 0.209
No. atoms	997	1076
Protein	847	949
Heme	43	43
Carbene	7	
Water	100	83
B factors	15.67	23.62
Protein	12.95	23.09
Heme	16.36	16.00
Carbene	26.17	
Water	37.66	33.57
R.M.S. deviations		
Bond lengths (Å)	0.002	0.017
Bond angles (°)	1.814	1.719

[a] Data were collected on a single crystal

[b] Values in parentheses are for highest-resolution shell.

Table S1B. Bond lengths of interest.

Crystal Structure	Fe–N(Imz) (Å)	Fe–O (Å)	Fe–C (Å)
6CUK	2.0	2.1	N/A
6CUN	2.1	N/A	1.9
Fe(TPFPP)(CPh_2)(MeIm)	2.17	N/A	1.83

Figure S1. Active-site front loop deviation. The active site front loop in *Rma* TDE is substantially deviated from its positioning in wild-type *Rma* cyt *c*.

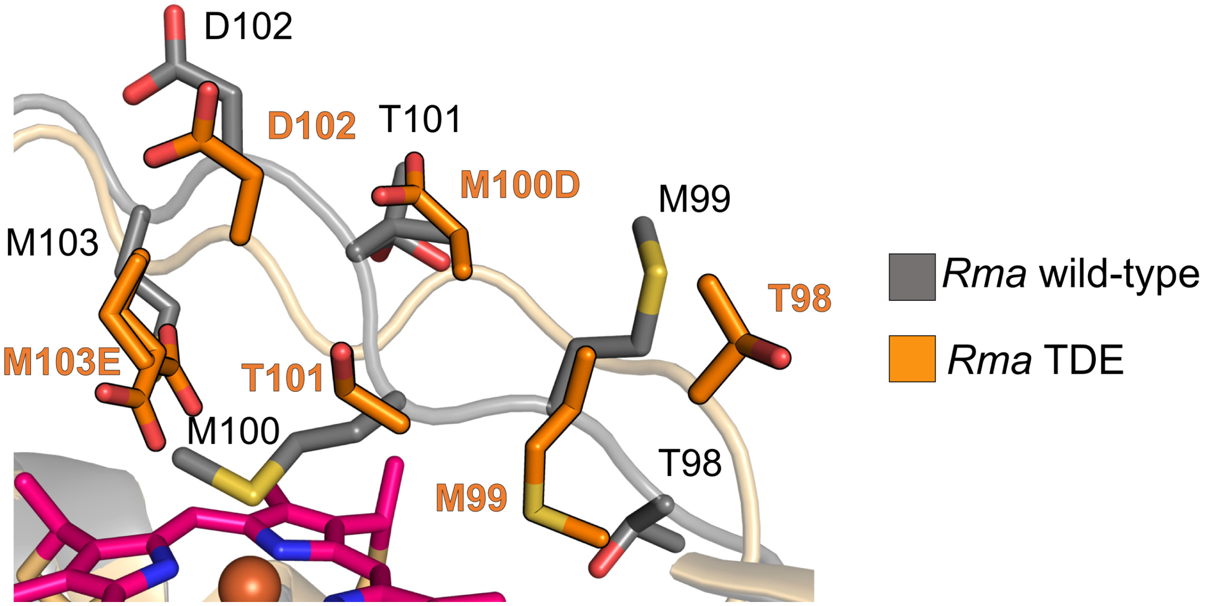

A. **Alignment of Rma wild-type (PDB: 3CP5) and *Rma* TDE (PDB: 6CUK).** The two structures superimposed on each other show that residues 98, 99, 100, and 101 have shifted the projection of their sidechains by approximately 180 degrees.

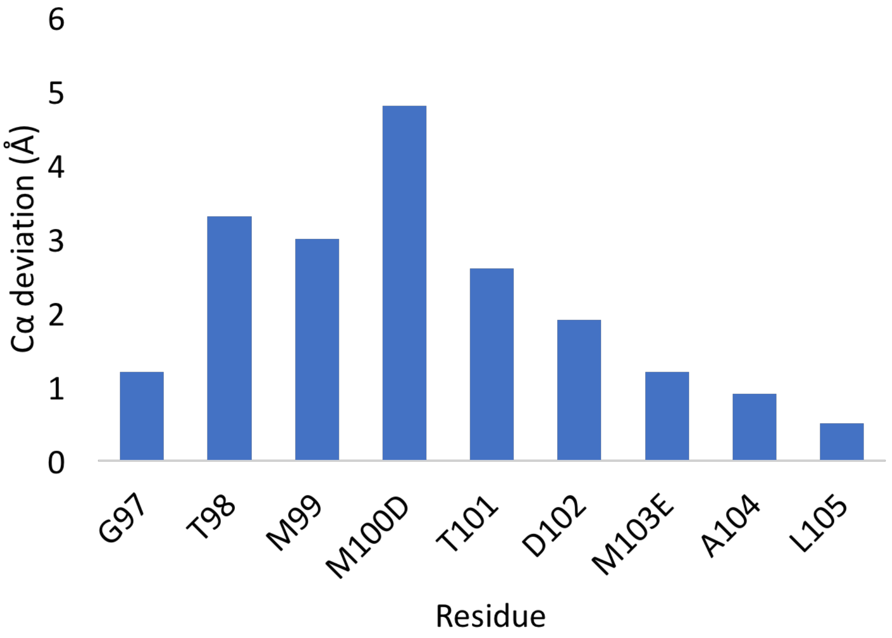

B. **Measurement of alpha-carbon deviations between *Rma* wild-type (PDB: 3CP5) and *Rma* TDE (PDB: 6CUK).** Distances were measured between the corresponding alpha carbons in wild-type *Rma* cyt *c*, and *Rma* TDE. The deviation measurements show that T98, M99, M100D, and T101 are substantially different in the two structures, with the largest deviation observed between M100 and D100 (4.8 Å).

Figure S2. UV-Vis spectra. UV-Vis spectra of reduced *Rma* TDE taken with and with and without the presence of the carbene precursor Me-EDA show that the spectrum changes upon addition of the carbene precursor.

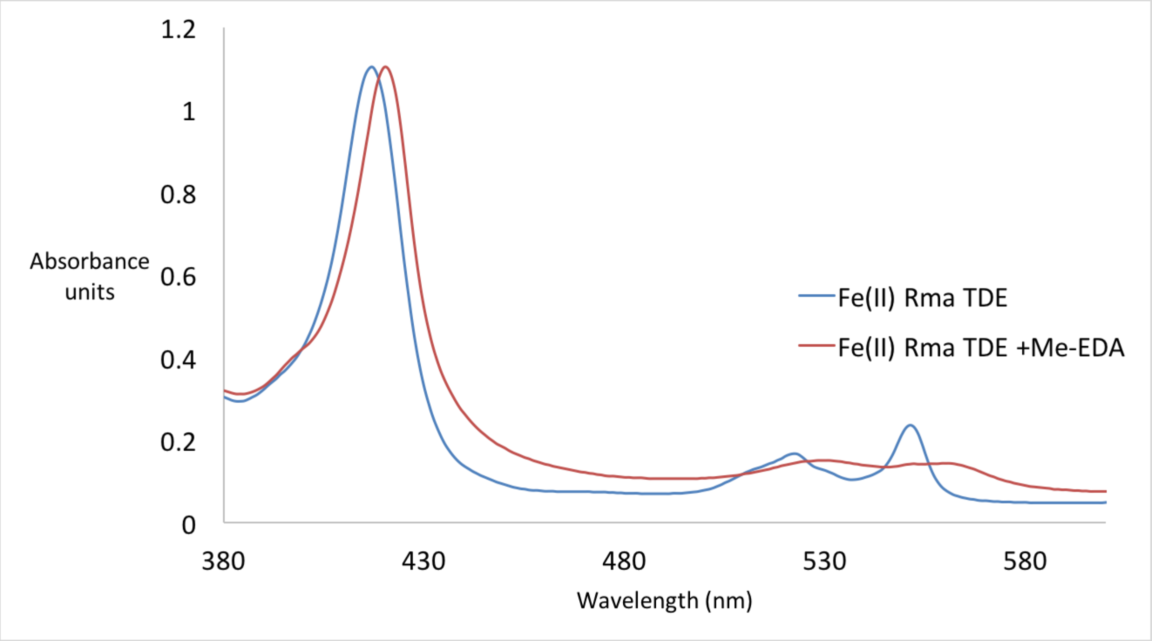

A. Aerobic spectra of reduced *Rma* TDE, and reduced *Rma* TDE treated with Me-EDA. The UV-Vis spectra of 7 μM reduced *Rma* TDE and 7 μM reduced *Rma* TDE, treated with Me-EDA were taken under the ambient atmosphere. The reduced spectrum shows a Soret band at 419 nm, a Q-band peak at 551 nm, and a Q-band minimum at 534 nm. The Me-EDA treated sample shows a Soret band at 416 nm, and two Q-band peaks at 529 and 561 nm. Previously characterized small- molecule IPC complexes have Soret bands at 403-408 nm and two Q-bands at 522-525 nm and 550-556 nm (61).

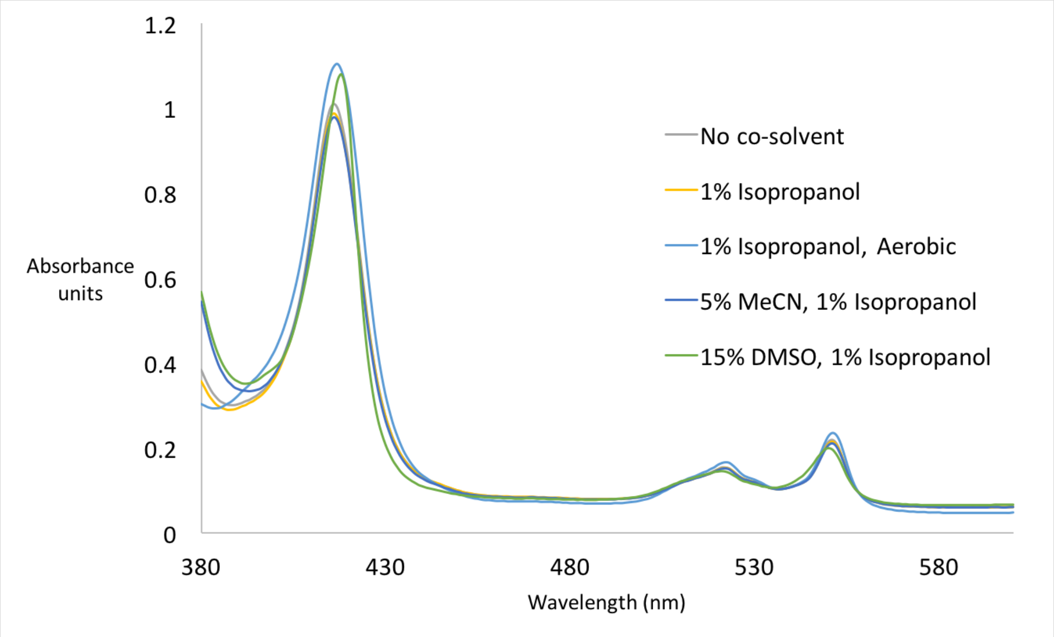

B. Spectra of reduced *Rma* TDE under various conditions. The UV-Vis spectra of 7 µM reduced *Rma* TDE were taken in the presence of various solvents, and unless specified, under an argon atmosphere. The reduced spectra show no substantial differences with the presence of isopropanol, acetonitrile (MeCN), or dimethylsulfoxide (DMSO). The spectrum also appears to undergo no substantial changes between an aerobic atmosphere and an argon atmosphere.

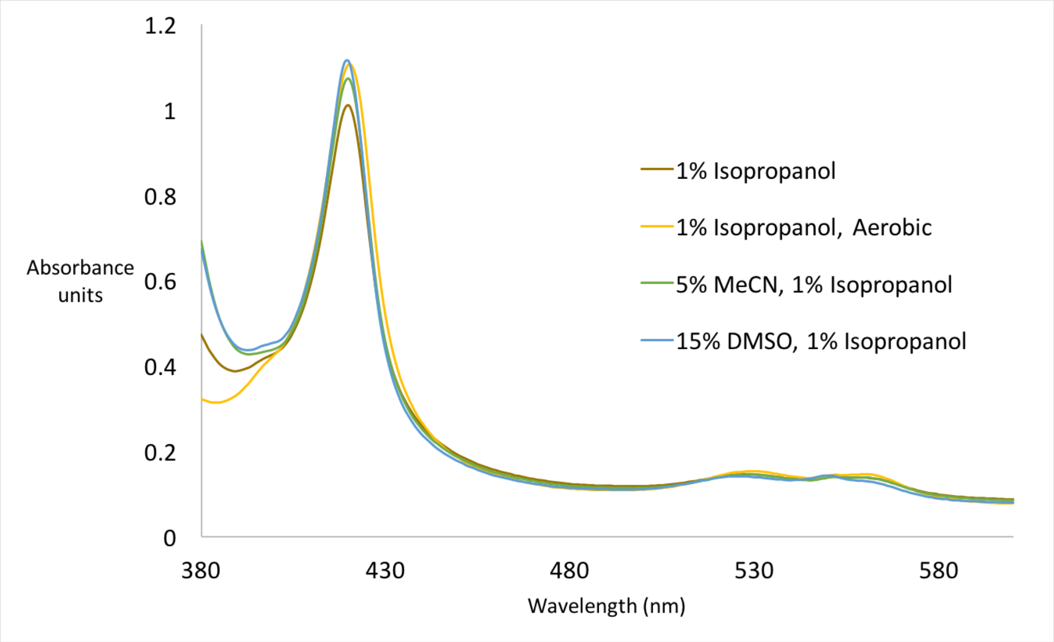

C. Spectra of reduced *Rma* TDE treated with Me-EDA under various conditions. The UV-Vis spectra of 7 µM reduced *Rma* TDE treated with Me-EDA were taken in the presence of various solvents, and unless specified, under an argon atmosphere. The spectra show no substantial differences with the presence of acetonitrile (MeCN) or dimethylsulfoxide (DMSO). The spectrum also appears to undergo no substantial changes between an aerobic atmosphere and an argon atmosphere.

Figure S3. EPR spectroscopic analysis.

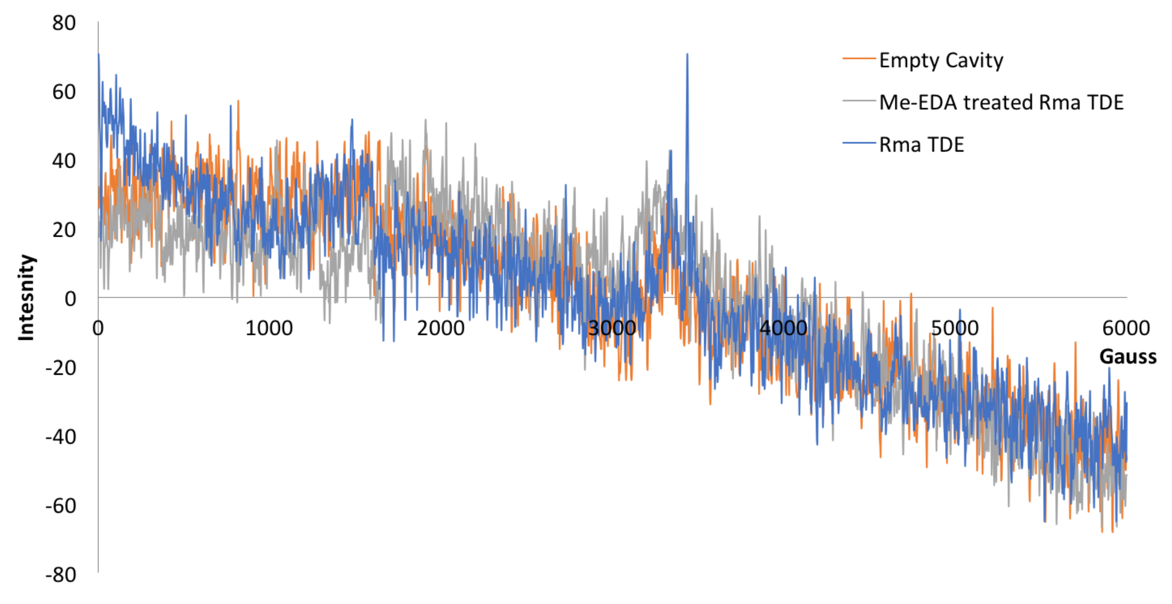

A. EPR spectra in perpendicular mode. The spectra for all three samples look highly similar. No signals are discernible from these spectra, indicating that the protein complexes present have integer spin states.

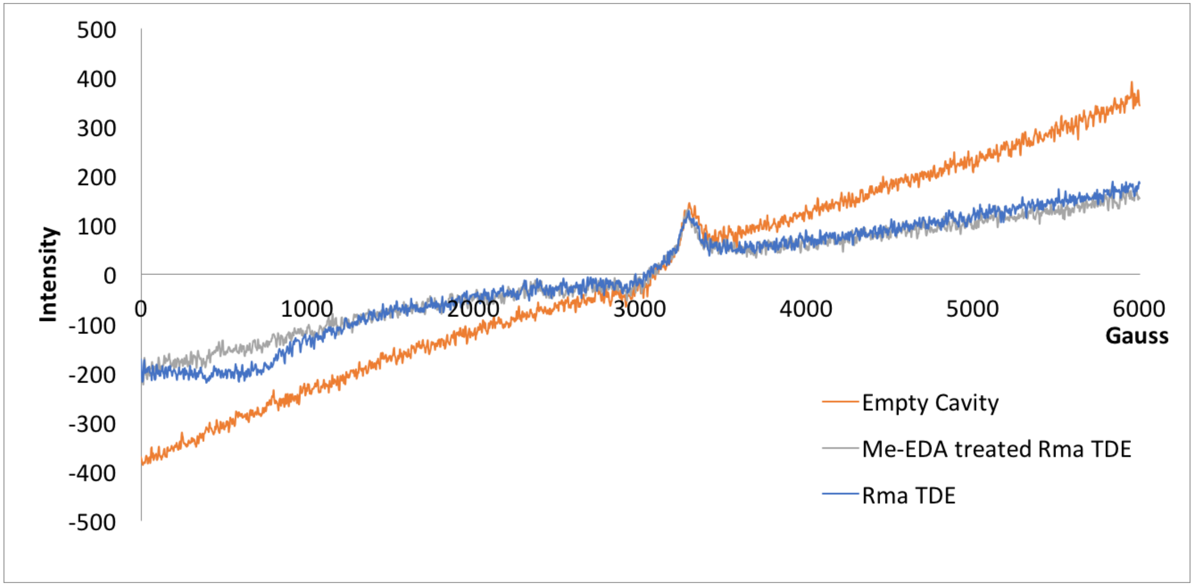

B. EPR spectra in parallel mode. The spectra for all three samples look highly similar. A signal is observed (at ~3300 Gauss) in all three spectra, including the empty cavity spectrum, which suggests this signal does not come from the protein. The observed signal is likely due to Cu(II) salts formed in the instrument as a result of oxidized conductors. Another small signal is observed (at ~800 Gauss) in the *Rma* TDE spectrum. This signal is typical of high spin Fe(II), but due to its low intensity, the signal likely comes from a small amount of Fe(II) contamination in the spectrum, rather than from *Rma* TDE. The lack of substantial protein-derived signal suggests that both protein complexes may be in low-spin states.

Figure S4. Mössbauer spectroscopy studies.

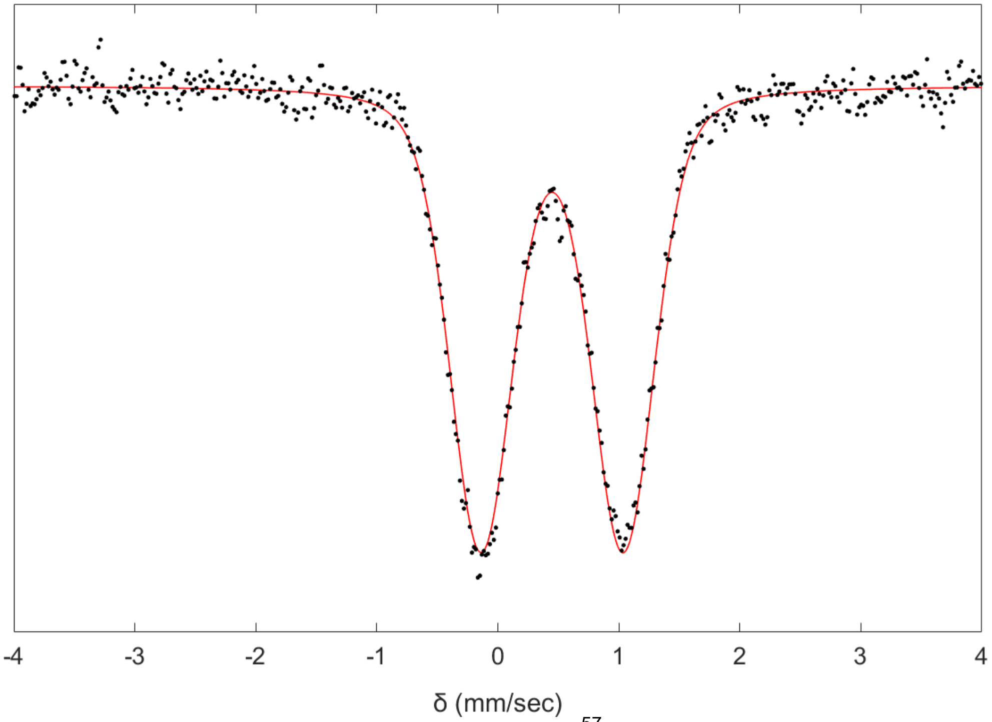

A. Zero-field Mössbauer spectrum at 80 K of ^{57}Fe-protein (3.8 mM) in frozen NaPi (19 mM, pH 7.5) and MeCN (5% v/v) in the presence of sodium dithionite (50 mM).

Fitting details for Figure S4.A. This Mössbauer was modelled as one species with the parameters seen below. In this case, the data was best fit using a Voigtian lineshape. The Voigtian lineshape is a Gaussian distribution of the typical Lorentzian lineshape observed in Mössbauer spectra. Although less typically observed for solution samples, small differences in the protein (e.g. folding), in the local active-site environment (e.g. solvent, H-bonding network), or small domains in the sample caused by rapid freezing could all result in such a lineshape. Alternative fits such as asymmetric Lorentzian lineshapes or adding in a second component lead to worse fits. Application of a small magnetic field (50 mT, Figure S4.B) rules out incipient magnetic behavior as the cause of this behavior. The isomer shift and quadrupole splitting of this species are in agreement with its assignment as a *S* = 0, heme species[62].

Component	**δ (mm s^{-1})**	**ΔE$_Q$ (mm s^{-1})**	**Linewidths, Γ$_L$/ Γ$_R$ (mm s^{-1})**
Red line	0.45 ± 0.02	1.18 ± 0.02	−0.60/−0.60

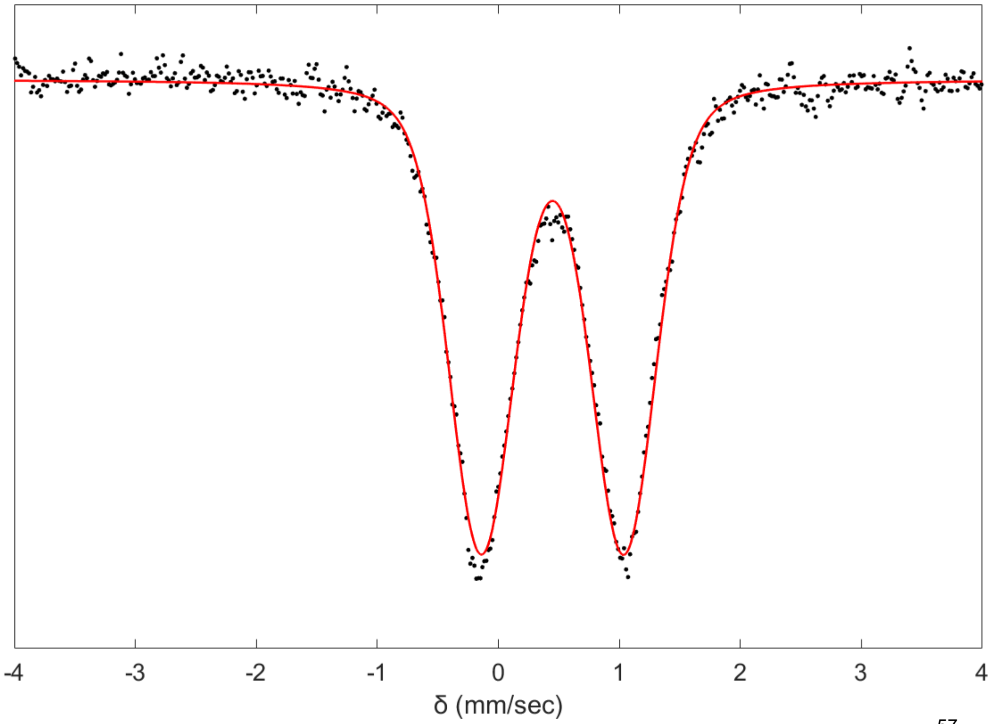

B. Parallel applied 50-mT magnetic field Mössbauer spectrum at 80 K of ^{57}Fe-protein (3.8 mM) in NaPi (19 mM, pH 7.5) and MeCN (5% v/v) in the presence of sodium dithionite (50 mM).

Fitting details for Figure S4.B. As expected given the proposed diamagnetic nature of this species, the application of a small magnetic field does not result in any changes to the signal observed in the zero-field spectrum.

Component	**δ (mm s^{-1})**	**ΔE_Q (mm s^{-1})**	**Linewidths, Γ_L/ Γ_R (mm s^{-1})**
Red line	0.45 ± 0.02	1.18 ± 0.02	−0.63/−0.63

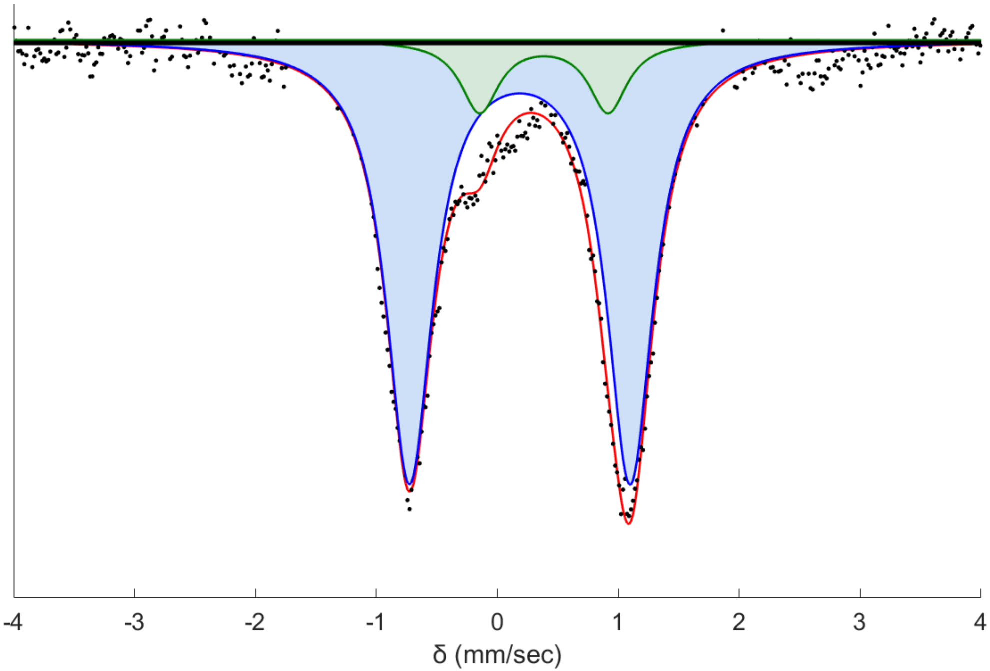

C. Zero-field Mössbauer spectrum at 80 K ^{57}Fe-protein (3.8 mM) in frozen NaPi (19 mM, pH 7.5) and MeCN (5% v/v) in the presence of sodium dithionite (50 mM) and Me-EDA (50 mM).

Fitting details for Figure S4.C. This Mössbauer was modelled as two species. The minor component is clearly defined by the absorbance feature at approximately −0.1 mm/sec. This fixes one half of that quadrupole doublet. The other absorbance is not clearly defined with respect to the major feature so the exact isomer shift and quadrupole splitting of this component is not well-defined. This is reflected in the slightly different parameters that are found for this feature in the spectrum taken with a 50 mT magnetic field applied. However, the fit featured here is reasonable for an Fe(II), *S* = 0 heme species which could be starting material, a reaction intermediate, or a carbene decomposition product. Forcing this feature to have the parameters of the *S* = 0 Fe(II) starting material (δ_{Fe} = 0.45 and $|\Delta E_Q|$ = 1.18) shown in Table S4.B did not substantially change the quality of the curve-fitting. To avoid over-interpretation this fit has not been enforced. The major absorbance is in agreement with Mössbauer parameters previously reported for formally Fe(IV), *S* = 0 heme species. (62)

Component	**δ (mm s^{-1})**	**ΔE_Q (mm s^{-1})**	**Linewidths, Γ_L/ Γ_R (mm s^{-1})**	**Relative area**
A (blue)	0.18 ± 0.02	1.83 ± 0.04	0.46/0.46	0.88
B (green)	0.38 ± 0.02	1.06 ± 0.02	0.38/0.38	0.12

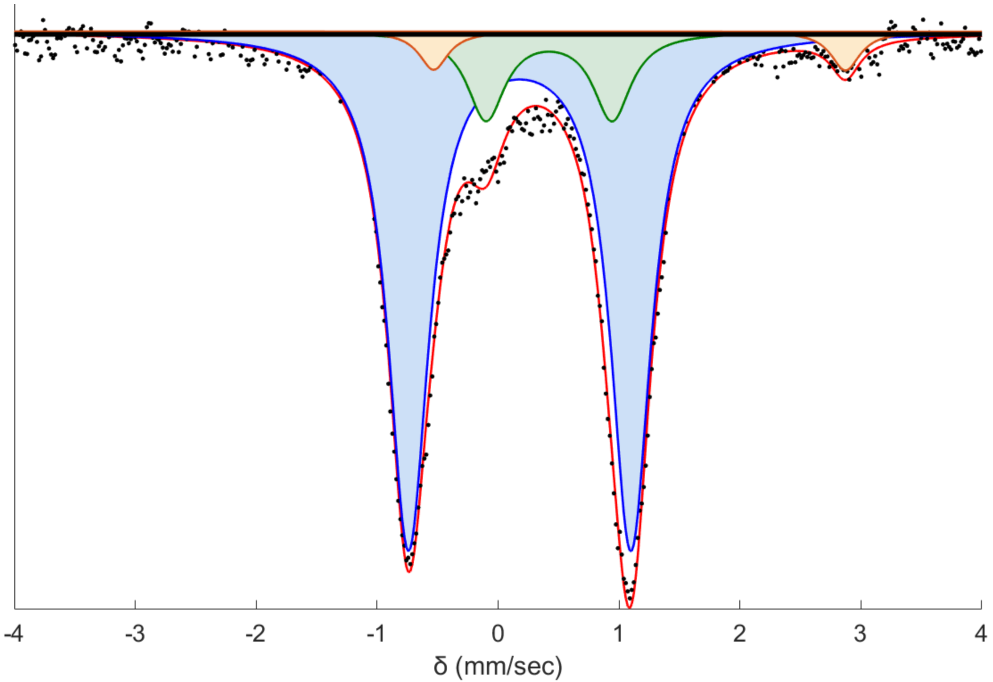

D. Parallel applied 50-mT magnetic field Mössbauer spectrum at 80 K of ^{57}Fe-protein (3.8 mM) in frozen NaPi (19 mM, pH 7.5) and MeCN (5% v/v) in the presence of sodium dithionite (50 mM) and Me-EDA (50 mM).

Fitting details for Figure S4.D. This Mössbauer was modelled as three species. Again, the major component (modelled in blue) is consistent with a *S* = 0, formally Fe(IV) heme species. Again, there is a second species as seen in Figure S4.C (modelled in green) that shows parameters consistent with an *S* = 0, Fe(II) impurity. The third species here (modelled in orange) has isomer shift and quadrupole splitting characteristic of high-spin (*S* = 2) Fe(II) that is likely not bound to the heme. This species may be poorly resolved due to broadening in the absence of the applied magnetic splitting explaining why it is not seen in Figure S4.C.

Component	**δ (mm s^{-1})**	**ΔE_Q (mm s^{-1})**	**Linewidths, Γ_L/ Γ_R (mm s^{-1})**	**Relative area**
A (blue)	0.18 ± 0.02	1.84 ± 0.04	0.41/0.41	0.82
B (green)	0.42 ± 0.02	1.04 ± 0.02	0.38/0.38	0.13
C (orange)	1.17 ± 0.02	3.40 ± 0.07	0.29/0.29	0.04

E. Comparison of Calculated and Experimental Mössbauer parameters

Entry Number	System	Method	Electronic state[c]	∂_{Fe} (mm/s)	ΔE_Q (mm/s)	Reference
1	*Rma* TDE (CMeCOOEt)	Experimental	CSS	0.18	(-)[a] 1.83	(This work)
2	Fe(Por)(CPh_2)(MeIm)	Calculated	CSS	0.19	-1.76	Khade *et al.* (63)
3	Fe(TPFPP)(CPh_2)[b]	Experimental	CSS	0.03	(-)[a] 2.34	Li *et al.* (61)
4	Fe(Por)(CPh_2)	Calculated	CSS	0.10	-2.37	Khade *et al.* (63)
5	Fe(Por)(CMeCOOEt)(Im) - wat [d]	Calculated	OSS	0.23	-1.06	(This work)
6	Fe(Por)(CMeCOOEt)(Im)- wat [d]	Calculated	CSS	0.20	-1.04	(This work)
7	Fe(Por)(CMeCOOEt)(Im) - wat [d]	Calculated	Triplet	0.24	-1.58	(This work)
8	Fe(Por-ext)(CMeCOOEt)(Im) [e]	Calculated	OSS	0.23	-1.21	(This work)
9	Fe(Por-ext)(CMeCOOEt)(Im) [e]	Calculated	CSS	0.21	-1.22	(This work)
10	Fe(Por-ext)(CMeCOOEt)(Im) [e]	Calculated	Triplet	0.30	-1.56	(This work)

Im = imidazole

[a] Sign not determined experimentally

[b] TPFPP = 5,10,15,20-Tetrakis(pentafluorophenyl)porphyrin

[c] CSS = Closed-shell singlet, OSS = Open-shell singlet

[d] Fe(Por)(CMeCOOEt)(Im) – wat = DFT optimized geometries for a truncated computational model that includes a H-bonded water molecule, see description as shown in Figure S9.

[e] Fe(Por-ext)(CMeCOOEt)(Im) = Truncated computational model that includes all the QM-region atoms from QM/MM optimized structures described in Figure S10.

The major species in Me-EDA treated *Rma* TDE was present at 88% abundance, a similarly high occupancy to that of the carbene observed in the crystal structure. This major species was best fit with $\partial_{Fe} = 0.18$ mm·s^{-1} and $|\Delta E_Q| = 1.83$ mm·s^{-1} (Figure S4.E, Entry 1). Although the isomer shift is higher than those typically observed for Fe(IV)–oxo species, the negative shift relative to the starting material is indicative of a short Fe−C bond. Additionally, the quadrupole splitting lies between the values typically observed for Fe(IV)–oxo species (1-1.5 mm·s^{-1}) and the values typically observed for Fe(IV)–hydroxo species (2-2.1 mm·s^{-1}) (64,65,66). Unlike the oxo species, both the hydroxo and carbene species are axially dissymmetric (d_{xz} and d_{yz} are no longer equivalent) and therefore are expected to display larger quadrupole splittings. Thus, based on its high occupancy and distinctive Mössbauer parameters, we conclude that the major species observed in the Me-EDA-treated sample is carbene-bound *Rma* TDE.

Previously, Khade and Zhang created a model of the IPC Fe(Por)(CPh_2) in a closed shell singlet state and simulated its Mössbauer parameters (Figure S4.E, Entry 3). Their simulations yielded numbers similar to those obtained experimentally for the complex Fe(TPFPP)(CPh_2) (Figure S4.E, Entry 4). Khade and Zhang also predicted parameters for the *N*-methylimidazole-ligated version of this complex, Fe(Por)(CPh_2)(MeIm) (Figure S4.E, Entry 2). We find that the Mössbauer parameters observed in our *Rma* TDE system (Entry 1) are similarly consistent with the parameters predicted for the imidazole-ligated IPC complex.

Our efforts to simulate Mössbauer parameters for our complex (Entries 5-7; and 8-10) yielded results that were insufficient to assign a definitive electronic state. Although further experimental characterization such as high-field Mössbauer or SQUID magnetometry would have to be conducted to unambiguously assign the spin state, the data thus far suggest that the enzyme IPC, like small molecule IPC complexes, exists in a singlet state.

F. Comparison of sample preparation conditions between Mössbauer samples and biocatalytic reaction samples

Component	Final concentration in Me-EDA Mössbauer sample	Final concentration in biocatalytic reaction sample
Rma TDE	3800 μM	2.0 μM
NaPi, pH 7.5	19 mM	19 mM
Sodium dithionite	50 mM	10 mM
Me-EDA	50 mM	10 mM
Dimethylphenylsilane	0 mM	10 mM
Acetonitrile	5% (v/v)	5% (v/v)

To demonstrate the catalytic relevance of the captured carbene species, Mössbauer samples were prepared under conditions similar to those used to assay the activity and enantioselectivity of *Rma* TDE. The same buffer system and co-solvent were used for both the biocatalytic samples and the Mössbauer samples. Increased concentrations of purified *Rma* TDE protein were necessary in the Mössbauer samples to achieve sufficient signal. Similarly, the concentration of sodium dithionite was increased in the Mössbauer samples to ensure complete reduction of the protein, and the concentration of the carbene-precursor Me-EDA was also increased to ensure that the protein was subjected to multi-turnover conditions, with excess carbene precursor.

Table S2. Out-of-plane heme distortion parameters for various IPC structures. Normal-Coordinate Structural Decomposition (NCS) quantitative analysis of the out-of-plane heme deformations using vibrational normal coordinates and complete-basis, as proposed by Jentzen and Shelnutt (67), and implemented in the online script by Liptak and co-workers (68). The out-of-plane normal deformations considered are: mean deviation out-of-plane (Doop), saddling (B2u), ruffling (B1u), doming (A2u), waving (Eg(x), Eg(y)), and propellering (A1u). Values are given in Å. The values used for discussion in the manuscript are highlighted in bold.

Species	**Doop**	**Saddling B2u**	**Ruffling B1u**	**Doming A2u**	**Waving (x) Eg(x)**	**Waving (y) Eg(y)**	**Propellering A1u**
Rma TDE[a]	**0.709**	0.162	0.620	0.115	0.037	0.277	0.016
Carbene-bound *Rma* TDE[b]	**0.603**	0.243	0.491	0.164	0.099	0.162	0.026
DFT-optimized model closed-shell singlet state	0.572	0.289	0.373	0.308	0.048	0.056	0.070
DFT-optimized model open-shell singlet state	0.426	0.001	0.421	0.062	0.015	0.009	0.001
DFT-optimized model triplet state	0.789	0.010	0.784	0.078	0.011	0.018	0.001
QM/MM optimized closed-shell singlet state	0.572	0.289	0.373	0.308	0.048	0.056	0.070
QM/MM optimized open-shell singlet state	0.586	0.296	0.396	0.298	0.051	0.055	0.071
QM/MM optimized Triplet state	0.601	0.325	0.408	0.282	0.030	0.069	0.067
Fe(TPFPP)(CPh_2)(MeImz)[b]	**1.028**	0.345	0.744	0.078	0.046	0.615	0.019

[a] Measured from 6CUK PDB structure.

[b] Measured from 6CUN PDB structure.

[b] Measured from 1208784.cif crystal structure reported in (61)

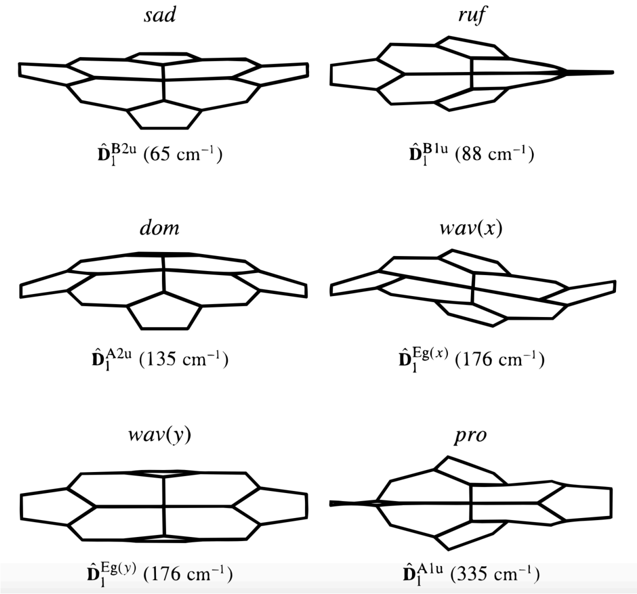

Representation of 1 Å displacements along the lowest-frequency, normal coordinate out-of-plane deformations used in the description of the nonplanar distortions of heme. (Reproduced from reference 67)

Out-of-plane distortion analysis on *Rma* TDE with and without the carbene ligand showed that for both structures, the primary out-of-plane distortion is ruffling, although the structure without the carbene ligand (6CUK, 0.620 Å) displays more ruffling than the structure with the carbene ligand (6CUN, 0.491 Å). Among the truncated model DFT-optimized structures (described in Figure S5), the triplet state is the least consistent with the out-of-plane deviations observed in carbene-bound *Rma* TDE, as the saddling deviation of the triplet is much lower than is crystallographically observed (0.010 Å vs 0.243 Å), and the ruffling deviation is much higher than is crystallographically observed (0.784 Å vs 0.491 Å). When considering the optimized structures by QM/MM, which take into account conformational restraints imposed by the protein on porphyrin ruffling (see Figure S10), the out-of-plane distortion parameters for all three electronic structures are similar to that observed in the crystal structure due to the rigidity imposed by the protein to the heme.

Figure S5. DFT modelling of a truncated IPC model considering different electronic states. DFT optimized structures of a truncated IPC **1** model. Key distances, angles and dihedrals are given in angstrom (Å) and degrees (°), respectively. A table containing the relative stabilities of the different optimized species in terms of their electronic energy (ΔE), zero-point corrected energy (Δ(E+ZPE)), enthalpy (ΔH), Gibbs energy (ΔG), and quasi-harmonic corrected Gibbs energy (ΔG-qh) is reported. Values obtained at (U)B3LYP-D3(BJ)/Def2TZVP/PCM(diethyl ether)//(U)B3LYP/6-31G(d)+SDD(Fe)/PCM(diethyl ether) level. All energy values are given in kcal·mol^{-1}.

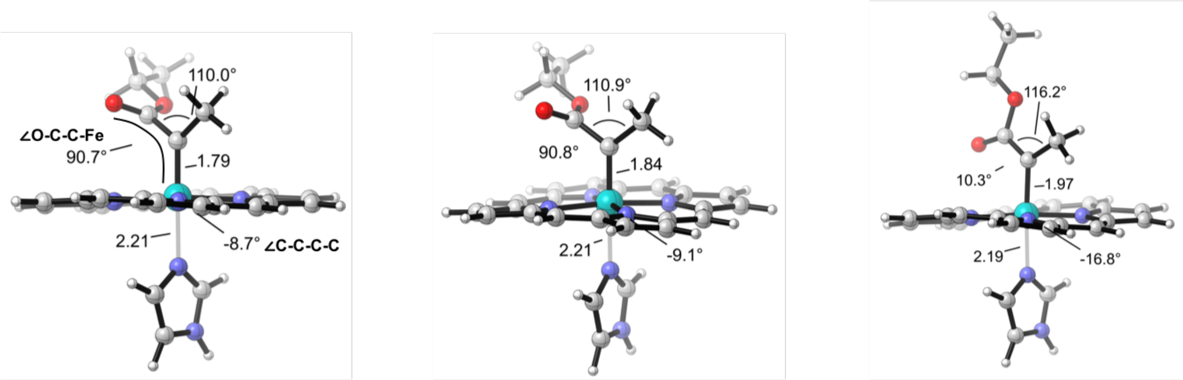

CSS OSS 3

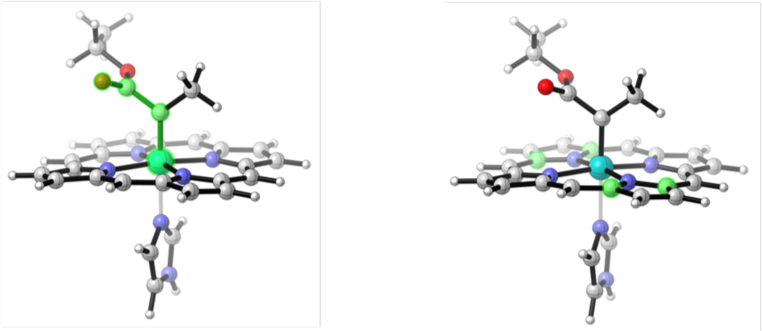

∠O-C-C-Fe dihedral angle ∠C-C-C-C ruffling dihedral angle

IPC 1 electronic state	ΔE	Δ(E+ZPE)	ΔH	ΔG	ΔG-qh
closed-shell singlet (CSS)	0.8	1.0	0.9	1.4	**1.0**
open-shell singlet (OSS)	0.0	0.0	0.0	0.0	**0.0**
triplet (3)	10.9	10.6	10.7	9.5	**9.8**

Energies in kcal·mol^{-1}.
All energy values discussed in the manuscript correspond to the quasi-harmonic corrected Gibbs energies (ΔG-qh) at (U)B3LYP-D3(BJ)/Def2TZVP/PCM(diethyl ether)//(U)B3LYP/6-31G(d)+SDD(Fe)/PCM(diethyl ether) level, if not otherwise noted.

Although different DFT functionals were tested during the development of the project (see discussion below), we have based our study on the use of the (U)B3LYP. B3LYP has been recently shown to provide accurate descriptions of the electronic configurations and geometries of iron porphyrin carbenes by the Shaik group (30) and non-heme iron carbene complexes by Luis and co-workers (31) in different computational studies on carbene transfer reactions.

DFT calculations showed that OSS (open-shell singlet) is lower in energy than the CSS (closed-shell singlet) by 1 kcal·mol^{-1}, and both singlet states are significantly more stable than the triplet state. The small energy difference between OSS and CSS is indicative that both electronic states could be possible, since the energy gap between them is within the DFT method error (see further discussion below).

In our current system, [Fe(Por)(Im)(CCH_3CO_2Et)] where Por = porphyrin, Im = imidazole; the optimized OSS and CSS structures are rather similar. The main differences come from the Fe–C bond distance, 1.84 Å in OSS and 1.79 Å in CSS. The enlargement of the optimized Fe–C bond is indicative of a decrease in bond order when moving from the closed-shell electronic state to the antiferromagnetically coupled biradical OSS. The Fe–C bond length is 1.97 Å in the triplet state.

An important observation when comparing the optimized geometries is the ester group adopts different conformations in different electronic states. In both singlet states, the ester group adopts a conformation parallel to the heme in order to reduce steric clashes. On the other hand, the ester conformation in the triplet state is rotated 90°, allowing stabilization of the unpaired electron on the carbene *p* orbital, which projects perpendicular to the carbene plane.

Our attempts to optimize an OSS geometry with a triplet-like ester conformation converged to the CSS-like ester conformation where the ester group is rotated (see Figure S5), even when starting from the optimized triplet structure geometry. This indicates that in our [Fe(Por)(Im)(CCH_3CO_2Et)] system, the stabilization of the radical on the carbene C atom in the OSS is mainly due to resonance provided by the substituting methyl group, and the release of steric clashes between the ester and porphyrin by rotation of the ester is more favorable than the extra stabilization provided by the ester conjugation (only possible in the triplet-like ester conformation). In the triplet state, the opposite is observed, and the ester is oriented to conjugate with the carbene radical. This latter observation is different from what was found by Shaik and co-workers when studying the [Fe(Por)(SCH_3)($CHCO_2Et$)] system (30). In their case, the ester group in the optimized OSS structure adopts the same conformation as in the triplet case, probably because of the lack of the stabilizing methyl group.

Another important difference between the optimized singlet vs. triplet geometries is observed in the porphyrin distortion, as discussed in Supporting Table S2, and clearly evidenced in the optimized structures represented in Figure S5. Although CSS and OSS exhibit small ruffling distortions of the porphyrin (ruffling B1u mode distortions 0.373 Å and 0.421 Å for CSS and OSS, respectively), the ruffling distortion in the triplet optimized geometry is much larger (the ruffling B1u mode distortion is 0.784 Å). This indicates that the IPC triplet state is better stabilized by a distorted porphyrin, opposite to CSS and OSS.

Spin contamination and stability test

The spin contamination in optimized OSS structures has been checked, having low $\langle S^2 \rangle$ values after annihilation (before annihilation 0.3827, after 0.0228). Single point calculations with the larger basis set (Def2TZVP) on optimized CSS geometries at (U)B3LYP/6-31G(d)+SDD(Fe) level failed the stability test, reinforcing the idea that CSS and OSS states are very close in energy and are very sensitive to IPC geometries, especially when they are not re-optimized at that particular level of theory.

DFT functional dependence on Singlet-Triplet (S-T) energy gaps

Early in our study we tested the performance of B3LYP functional in estimating the singlet-triplet (S-T) gap by comparing DFT functionals of different nature that contain different percentage of HF exchange. We fully optimized the truncated DFT model using 6-31G(d)+SDD(Fe) basis set and M06-L (meta-GGA with 0% HF), MN15-L (meta-NGA with 0% HF), B3LYP (hybrid GGA 20% HF), and M06 (hybrid meta-GGA with 27% HF) functionals. Our results showed that all tested functionals described the singlet spin state as lower in energy, with S-T gaps in the range of 5.8-12.9 kcal/mol (see table below). When doing single point calculations on these optimized geometries with the respective functionals and a larger basis set (Def2TZVP), the computed S-T energy gaps are estimated to be all within the range of 8.9-13.3 kcal/mol (see table below). Notice that ruffling in the triplet state is even larger with other functionals than in B3LYP (see optimized structures below).

DFT functional	**Optimizations: 6-31G(d)+SDD(Fe)/PCM(diethyl ether)**		**Single points on optimized geometries: Def2TZVP/PCM(diethyl ether)**	
	ΔE	**ΔG**[a]	**ΔE**	**ΔG**[a]
M06-L	12.8	**11.6**	11.3	**10.1**
MN15-L	15.1	**12.9**	15.5	**13.3**
B3LYP	7.8	**5.8**	10.9	**8.9**
M06	11.3	**10.1**	11.3	**8.9**

Energies in kcal·mol^{-1}.

[a] Non-corrected ΔG values.

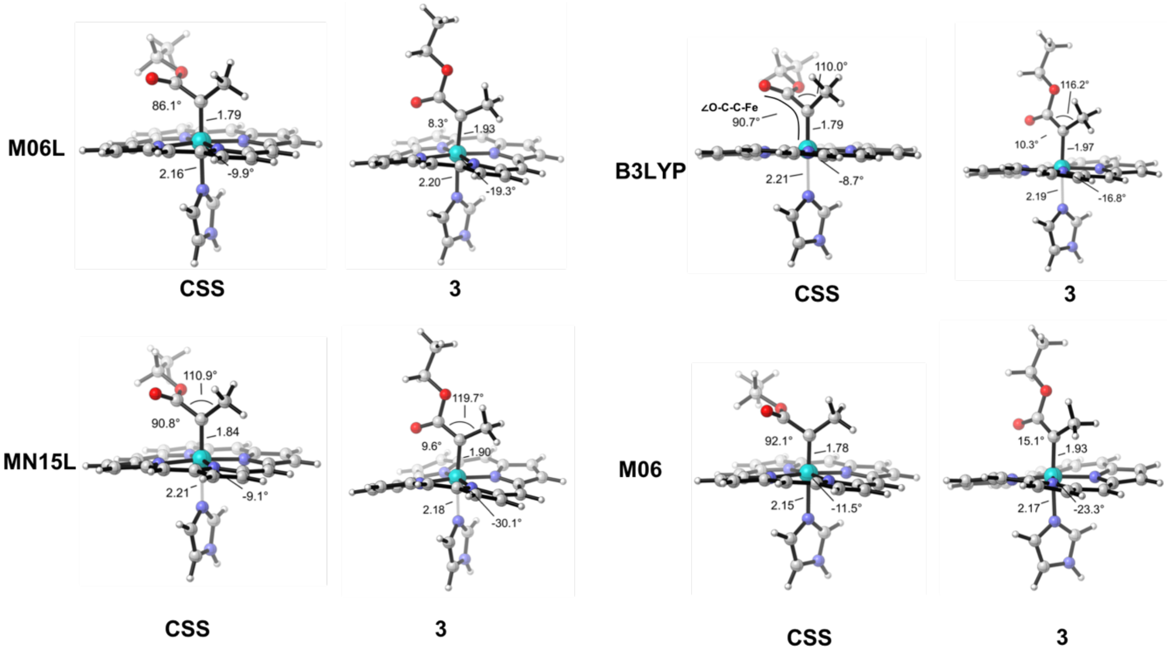

These results are in line with early tests carried out by Shaik and co-workers (30), where they proved the stability of B3LYP functional in describing the S-T energy gap in a related Fe-heme carbene complex against other DFT functionals (TPSSh, BMK in addition to M06-L and M06).

Figure S6. DFT modelling of (Fe,N)-bridged mode of truncated IPC model. DFT optimized structures of a truncated IPC **1** model in an (Fe,N)-bridged mode. Key distances, angles and dihedrals are given in angstrom (Å) and degrees (°). A table containing the relative stabilities of the different optimized species in terms of their electronic energy (ΔE), zero-point corrected energy (Δ(E+ZPE)), enthalpy (ΔH), Gibbs energy (ΔG), and quasi-harmonic corrected Gibbs energy (ΔG-qh) is reported. Values obtained at (U)B3LYP-D3(BJ)/Def2TZVP/PCM(diethyl ether)//(U)B3LYP/6-31G(d)+SDD(Fe)/PCM(diethyl ether) level. All energy values are given in kcal·mol^{-1}.

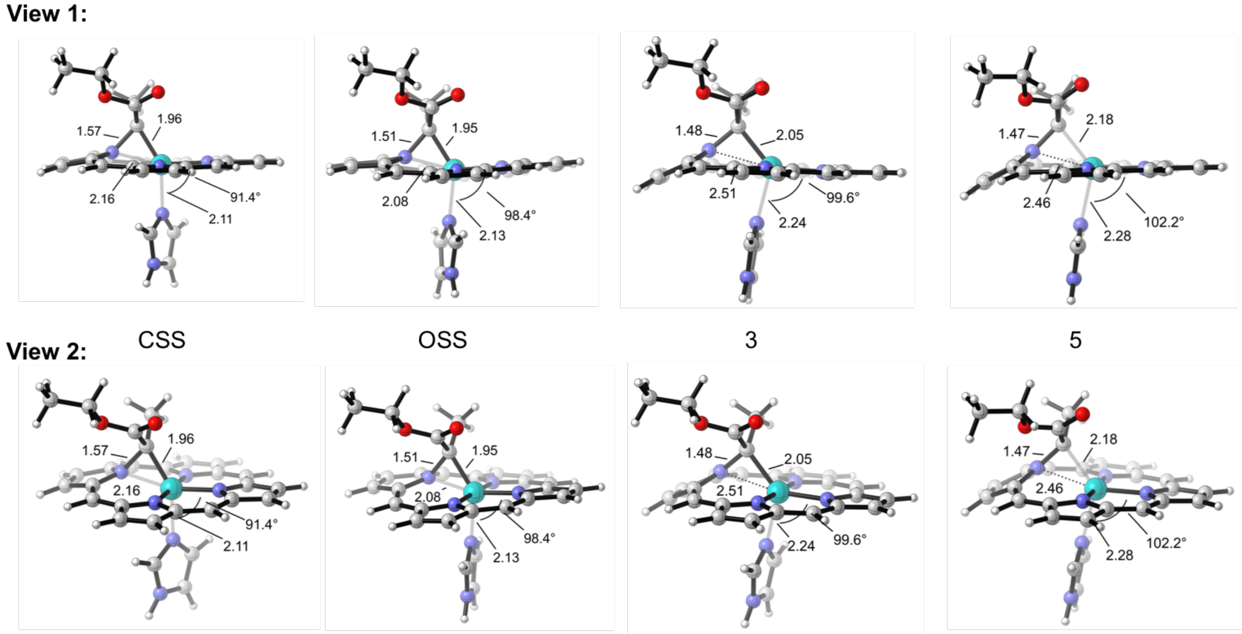

Carbene mode	Electronic state	ΔE	Δ(E+ZPE)	ΔH	ΔG	ΔG-qh
end-on	closed-shell singlet (CSS)[a]	0.8	1.0	0.9	1.4	**1.0**
	open-shell singlet (OSS)[a]	0.0	0.0	0.0	0.0	**0.0**
	triplet (3)[a]	10.9	10.6	10.7	9.5	**9.8**
(Fe,N)-bridged	closed-shell singlet (CSS)	19.2	20.0	19.4	21.4	**20.8**
	open-shell singlet (OSS)	14.7	15.5	14.9	17.0	**16.3**
	triplet (3)	11.3	11.6	11.3	11.7	**11.4**
	quintet (5)	14.4	13.6	13.6	12.8	**12.6**

Energies in kcal·mol^{-1}.

All energy values discussed in the manuscript correspond to the quasi-harmonic corrected Gibbs energies (ΔG-qh) at (U)B3LYP-D3(BJ)/Def2TZVP/PCM(diethyl ether)//(U)B3LYP/6-31G(d)+SDD(Fe)/PCM(diethyl ether) level, if not otherwise noted.

[a] Values from Supporting Figure S5, reported for comparison.

DFT calculations on IPC **1** model system showed that (Fe,N)-bridged carbene is thermodynamically much less stable than the end-on carbene mode, in all the studied electronic states. The most stable (Fe,N)-bridged carbene is more than 10 kcal·mol^{-1} higher in energy than the most stable end-on OSS.

(Fe,N)-bridged structures are better stabilized at higher spin states, with the triplet and the quintet states being the more stable bridged carbenes. It is worth mentioning that in the triplet state, the bridged mode is only 1.5 kcal·mol^{-1} higher in energy than the end-on triplet IPC. This suggests that the (Fe,N)-bridged carbene could only be accessible in the triplet state, while singlet open-shell and closed-shell electronic states clearly favor the end-on carbene geometry.

This is in contrast to what was found by Shaik and co-workers[30] for a similar IPC [Fe(Por)(SCH_3)($CHCO_2Et$)] system. Using an equivalent computational model for a cysteine axial ligated Fe-porphyrin, they found bridged carbenes were thermodynamically more stable than their corresponding end-on modes. The different trends observed in Shaik's and the work presented here indicate that the Fe axial ligand may play a role in controlling the relative stabilities of end-on vs. bridged carbene modes.

When comparing low spin (CSS and OSS) geometries to triplet and quintet ones, we observed that in CSS and OSS there is still a covalent bond between the porphyrin N and the iron center, while this bond is cleaved in the higher spin structures. Having this Fe–N bond in the carbene-bridging structure induces large strain on the structure, causing large destabilization. On the other hand, in the triplet and quintet optimized structures the Fe–N bond is cleaved, allowing the out-of-plane displacement of the porphyrin pyrrole ring, which can now better interact with the new quaternary bridging carbon from the carbene stabilizing this geometry. Thus, large distortions of the porphyrin are needed to stabilize the (Fe,N)-bridged mode, which are not possible in *Rma* TDE due to covalent linkage of the heme to the two cysteines (C45 and C48) that makes the porphyrin rigid.

Our computational results demonstrate that end-on carbenes are thermodynamically more stable than the (Fe,N)-bridged structure in our system, and that end-on carbenes favor singlet states, while (Fe,N)-bridged structures favor high-spin states. Experimentally, we observe an end-on carbene in the crystal structure, and spectroscopic characterization of the carbene is consistent with a singlet state. Therefore, we conclude that the (Fe,N)-bridged structures play no direct role in the catalytic cycle of carbene insertion into Si–H bonds.

Figure S7. Computational modelling of the carbene conformation in *Rma* TDE.

S7.A. DFT modelling of IPC rotation. Relaxed potential energy surface (PES) corresponding to the IPC **1** rotation coordinate, as defined by the N-Fe-C-C angle (highlighted atoms in the figure), using a truncated IPC model containing the porphyrin pyrrole core, Fe center, carbene and an imidazole Fe-axial ligand at (U)B3LYP-D3(BJ)/Def2TZVP/PCM(diethyl ether)//(U)B3LYP/6-31G(d)+SDD(Fe)/ PCM(diethyl ether) level.

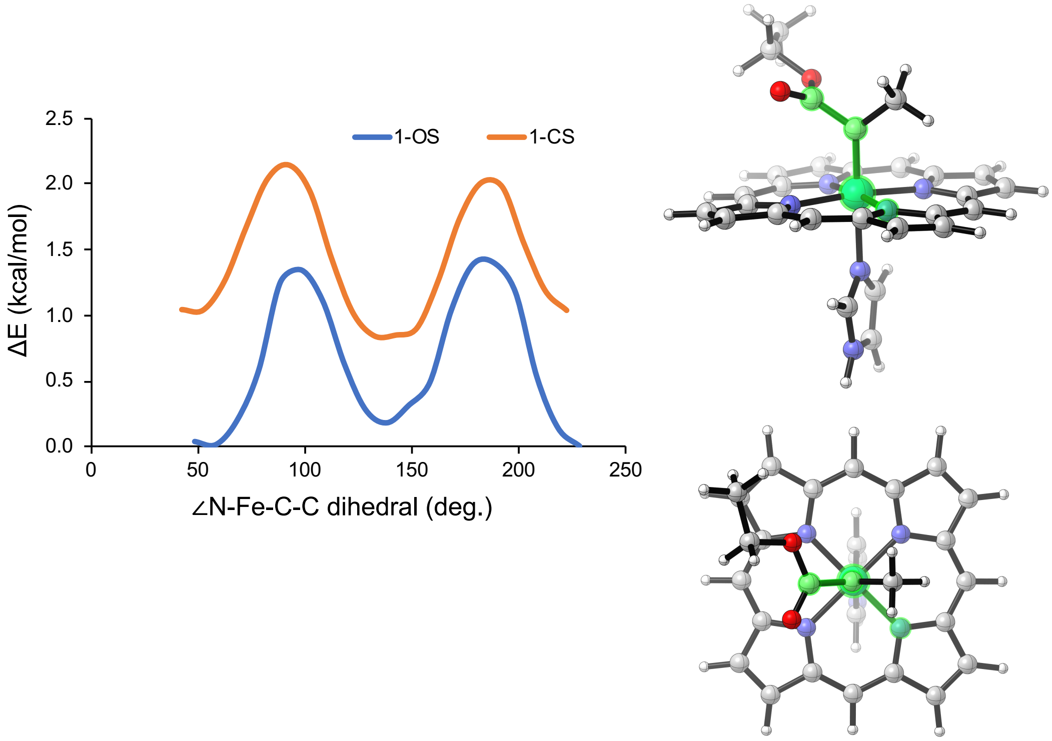

Calculations show that carbene rotation about the Fe–C bond is energetically feasible for both singlet closed-shell and singlet open-shell electronic states, with rotational barriers of about 1 kcal·mol^{-1}. This indicates that without steric constraints imposed by the protein environment or any (a)polar interaction with any surrounding residues, the carbene can explore any rotational conformer.

S7.B. *Rma* TDE carbene conformational analysis from independent Molecular Dynamics simulation trajectories. Molecular Dynamics (MD) simulations were applied to study the dynamic behavior of the IPC. To analyze the possible conformations explored by IPC **1** in *Rma* TDE, the **∠ N-Fe-C-C** dihedral angle (see description in the figure) was monitored along 5 independent MD trajectories of 1000 ns (1 μs) each (**a-f**).

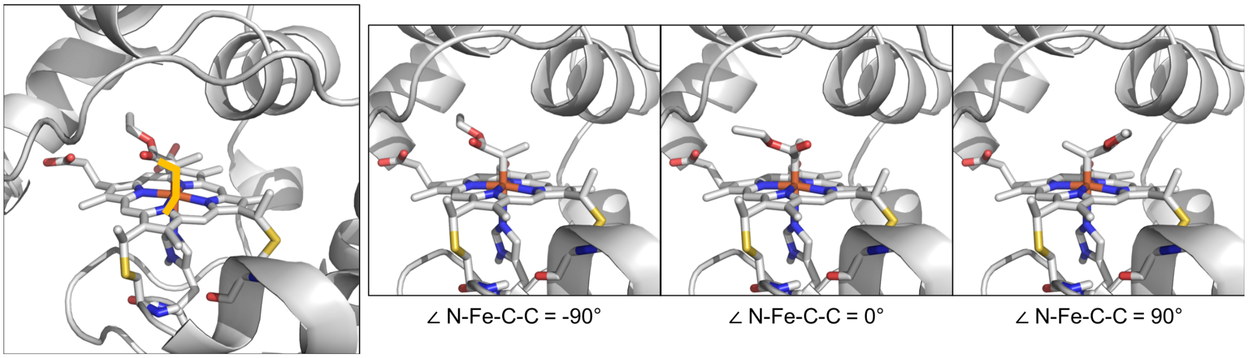

∠ N-Fe-C-C = -90°   ∠ N-Fe-C-C = 0°   ∠ N-Fe-C-C = 90°

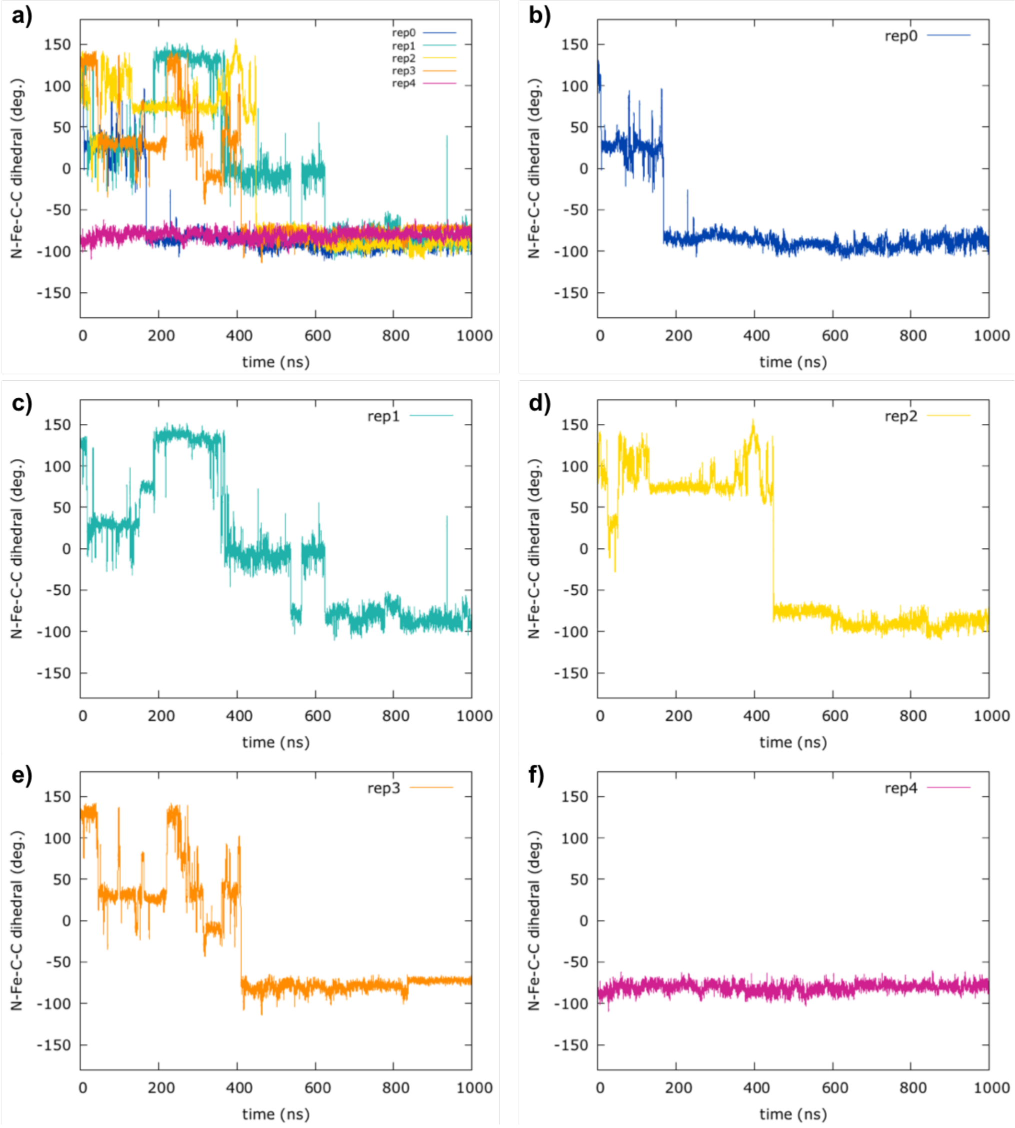

The starting carbene conformation for each independent simulation (5 simulations in total) was designed to be different, as represented by the different values of ∠ **N-Fe-C-C** angle at time = 0 ns in **a-f** plots for replicas 0 to 4. The conformation of IPC **1** where ∠ **N-Fe-C-C** values are around –90° corresponds to the carbene orientation found in the *Rma* TDE carbene-bound crystal structure. Our simulations revealed that, although different rotational conformations can be explored by the IPC during the different MD simulations, all 5 trajectories converge to the same carbene conformation with ∠ **N-Fe-C-C** values around –90° (plot **a**), consistent with the conformation observed in the X-ray crystal structure. Additional conformations are explored during simulations but are not persistent, indicating that these carbene conformations are not stabilized. The alternative conformations mainly explored by the carbene are: 1) where the ester group is pointing towards the front loop oriented to outside the active site (∠ **N-Fe-C-C** values around 0°) in replica 0 (plot **b**), replica 1 (plot **c**), and replica 3 (plot **e**); and 2) where the carbene is 180° rotated from the conformation in the x-ray structure, that is ∠ **N-Fe-C-C** has values around 90°, in replica 2 (plot **d**).

In all the trajectories, when the carbene reaches the ∠ **N-Fe-C-C** ~ -90° conformation, it remains until the end of the simulation. This indicates that the IPC is highly stabilized in that particular orientation. This is clearly exemplified by the trajectory in replica 4 (plot **f**), where the carbene already starts from that preferred conformation and does not explore any other possible orientation during the entire simulation time.

Despite the hydrophobic nature of the *Rma* TDE active site, and the lack of stabilizing interactions between the IPC and the surrounding protein residues in the carbene-bound crystal structure, MD simulations revealed the existence of a strong H-bond interaction between a water molecule that bridges the carbene ester and one carboxylic group from the heme (see discussion below). This strong interaction, not observed in the crystal structure because of the unresolved loop region, largely stabilizes the carbene in the ∠ **N-Fe-C-C** ~ -90° conformation during MD simulations, preventing its further rotation to explore other conformations.

S7C. Bridging water molecule during MD simulations. Active site views in snapshots taken every 150 ns from replica 0 MD simulation (Figure S7.B.b).

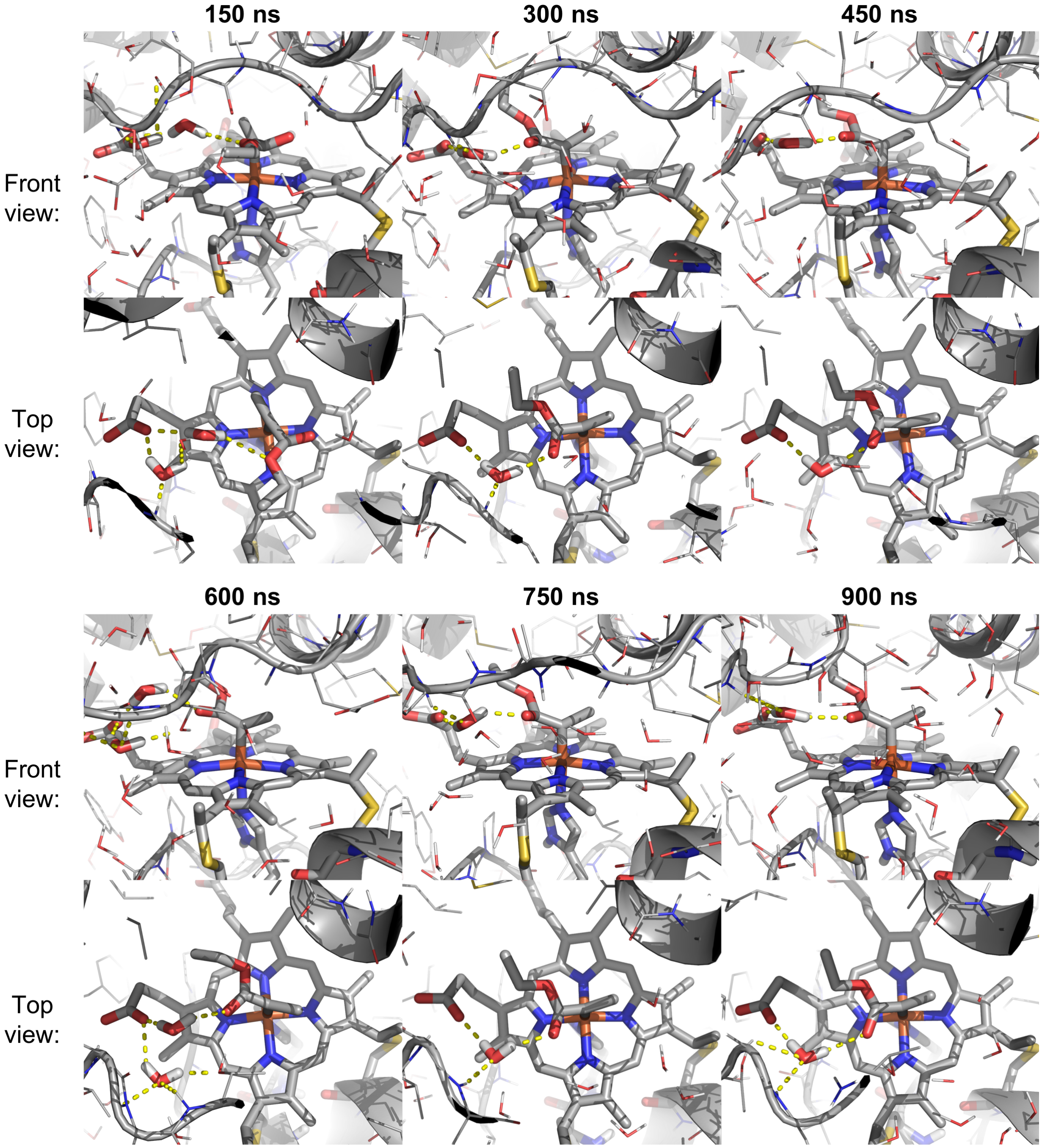

Snapshots, arbitrarily selected every 150 ns during the MD trajectory, provide evidence for the presence of a water molecule that strongly interacts with the carboxylate group of the heme during the entire simulation, independent of the carbene orientation (see for instance snapshots at t = 150 and 300 ns). Because the water is persistently present regardless of the orientation of the carbene, the water can be described as being pre-organized into the active site environment.

What is more interesting is that, when the carbene explores an orientation that resembles the one observed in the crystal structure (as described in Figure S7.B), the water molecule can establish strong H-bonding interactions with the carbonyl oxygen on the carbene ester group, as shown in snapshots at t = 300 and 750 ns. The water molecule, when bridging the heme carboxylate and the carbene, stabilizes the carbene IPC in this particular conformation. Once the carbene stabilizes these H-bonding interactions, it does not explore any other possible orientation during the entire simulation time, as described in Figure S7.B. Because the pre-organized water allows the enzyme to lock the IPC into a single conformation, the active site can be described as pre-organized for binding a single orientation of the IPC.

The position of the pre-organized water molecule can be further stabilized by polar interactions with the backbone front loop, especially with the backbone amide of D100. Nevertheless, these additional interactions are not essential for stabilizing the water molecule in this bridging position, as shown, for instance, in snapshots at t = 450 and 600 ns where the loop moves away due to its intrinsic flexibility.

Our MD simulations provide evidence that the presence of this bridging water molecule is the most important source of stabilization to keep the carbene in a single main orientation in solution, which has important implications for the catalytic activity of the enzyme.

Figure S8. DFT modelling of Si-H insertion transition states.

S8.A. DFT optimized structures of Si–H carbene insertion transition state (TSs) using a truncated IPC 1 model and dimethylphenylsilane, considering different possible electronic states. Key distances, angles and dihedrals are given in angstrom (Å) and degrees (°). A table containing the relative stabilities of the optimized TS in terms of their electronic energy (ΔE), zero-point corrected energy (Δ(E+ZPE)), enthalpy (ΔH), Gibbs energy (ΔG), and quasi-harmonic corrected Gibbs energy (ΔG-qh) is reported. Values obtained at (U)B3LYP-D3(BJ)/Def2TZVP/PCM(diethyl ether)//(U)B3LYP/6-31G(d)+SDD(Fe)/PCM(diethyl ether) level. All energy values are given in kcal·mol^{-1}.

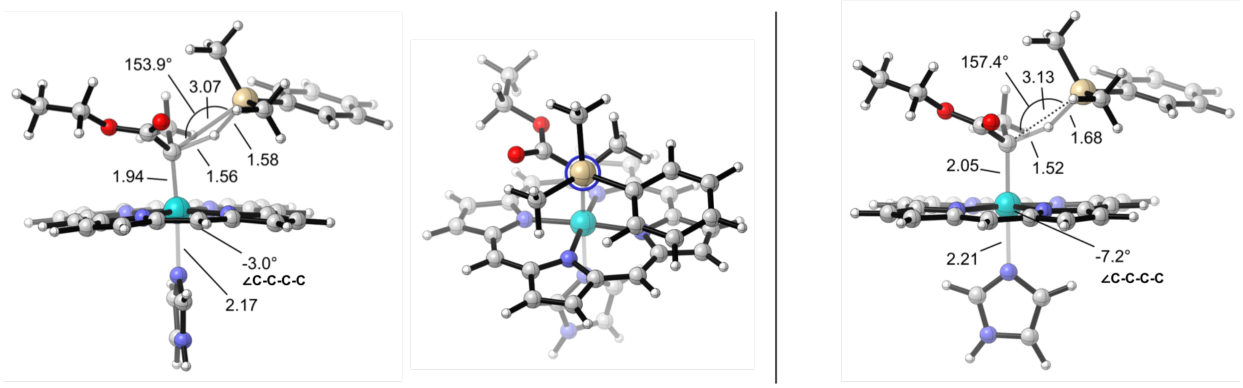

$\text{TS}^{\text{Si-H}}$-CSS

$\text{TS}^{\text{Si-H}}$-3

Electronic state	ΔΔE	ΔΔ(E+ZPE)	ΔΔH	ΔΔG	ΔΔG-qh
$\text{TS}^{\text{Si-H}}$-CSS (closed-shell singlet)	0.0	0.0	0.0	0.0	**0.0**
$\text{TS}^{\text{Si-H}}$-3 (triplet)	15.5	13.8	14.5	10.6	**12.5**

Energies in kcal·mol^{-1}.

All energy values discussed in the manuscript correspond to the quasi-harmonic corrected Gibbs energies (ΔG-qh) at (U)B3LYP-D3(BJ)/Def2TZVP/PCM(diethyl ether)//(U)B3LYP/6-31G(d)+SDD(Fe)/PCM(diethyl ether) level, if not otherwise noted.

DFT calculations on the model IPC **1** system showed that the lowest in energy Si–H insertion transition state (TS) corresponds to the closed-shell singlet state, which is 12.5 kcal·mol^{-1} lower in energy than the radical triplet TS. The open-shell singlet TS could not be optimized.

The optimized geometries also showed that the porphyrin is highly planar at the both the CSS and triplet transition states, as described by the ruffling C-C-C-C dihedral angle (as defined in Figure S5). Additionally, the TS structures described the optimal approach from the silyl substrate to the IPC **1**, where the phenyl ring and methyl groups on the silyl substrate are disposed in an alternate conformation with respect to the carbene to minimize steric clashes.

S8.B. Selectivity model for Si–H carbene insertions catalyzed by *Rma* TDE.

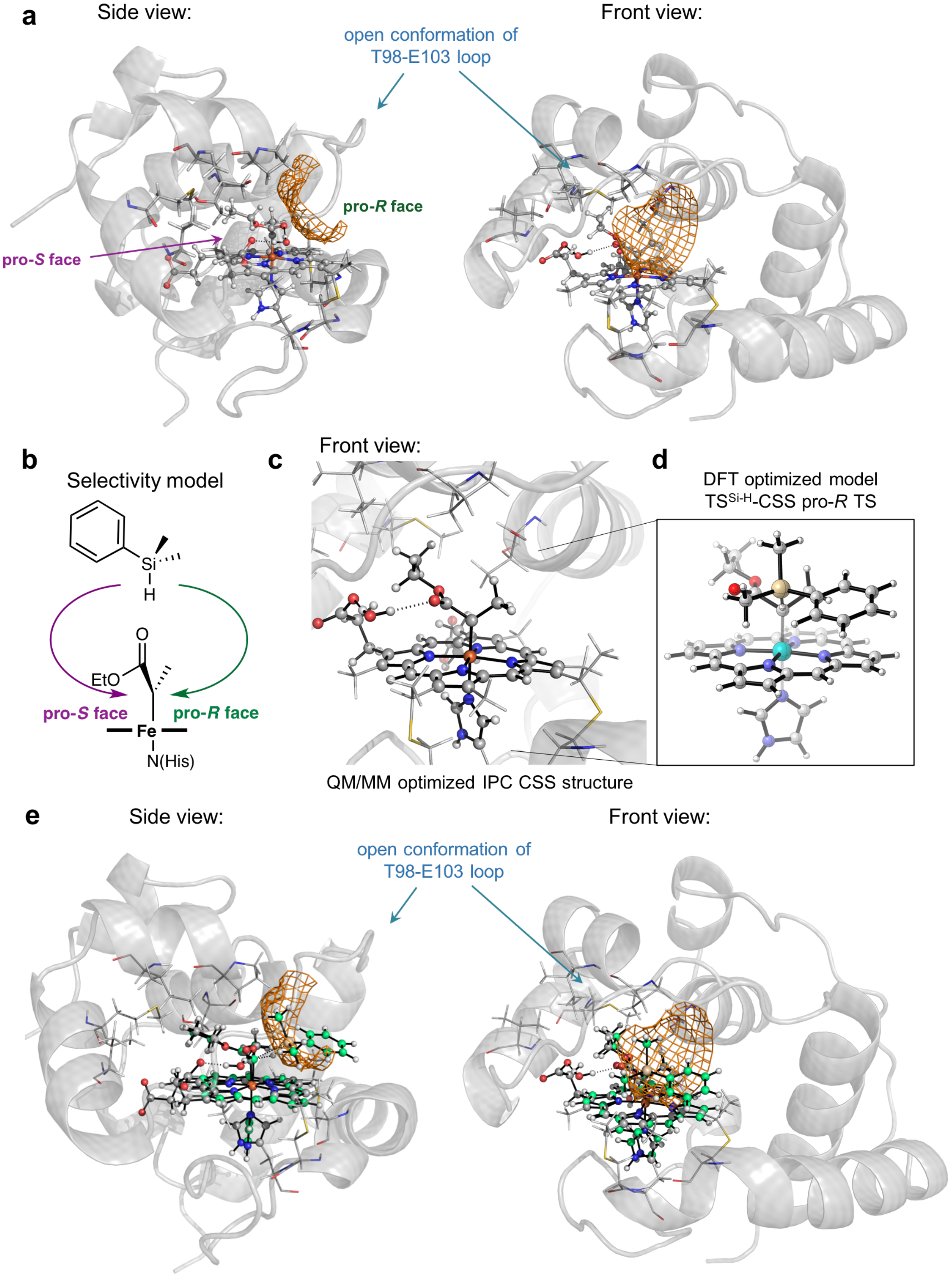

In Figure S8.B.**a** the solvent accessible surface of IPC **1** in the most populated cluster structure obtained from a 1000 ns MD trajectory, further optimized through QM/MM in its closed-shell singlet state (see Figure S10 for QM/MM modelling details) is shown in orange. From there, it is observed that only the pro-*R* face of the carbene is accessible for the silyl substrate (Figure S8.B.**b**), while the pro-*S* face of the IPC is blocked by surrounding protein residues and extensive hydrophobic contacts in this region. This is mainly due to two factors: 1) the stabilized conformation of the carbene in *Rma* TDE, as described in Figure S7; and 2) the flexibility of the front loop that can easily explore an "open" conformation, allowing the access of the second substrate to the IPC.

Comparison of the QM/MM optimized carbene geometry in the *Rma* TDE protein environment and the DFT modelled pro-*R* TS (Figures S8.B.**d** and S8.B.**e**) highlights that the carbene is highly pre-organization to interact with the substrate through a pro-*R* TS.

When superimposing both structures in Figure S8.B.**f**, the QM/MM optimized carbene geometry in the *Rma* TDE (in grey) and the DFT modelled pro-*R* TS (in green), the silyl substrate in the optimized transition state fits perfectly into the space made available (solvent accessible surface, in orange) when the *Rma* TDE front loop is in its "open" conformation. Thus, the high degree of flexibility of the front loop in *Rma* TDE is essential for stabilizing the pro-*R* transition state and achieving high selectivity.

Figure S9. DFT modelling of a truncated IPC model, stabilized by H-bonding with a water molecule. DFT optimized structures of a truncated IPC **1** model. Key distances, angles and dihedrals are given in angstrom (Å) and degrees (°). A table containing the relative stabilities of the different optimized species in terms of their electronic energy (ΔE), zero-point corrected energy (Δ(E+ZPE)), enthalpy (ΔH), Gibbs energy (ΔG), and quasi-harmonic corrected Gibbs energy (ΔG-qh) is reported. Values obtained at (U)B3LYP-D3(BJ)/Def2TZVP/PCM(diethyl ether)//(U)B3LYP/6-31G(d)+SDD(Fe)/PCM(diethyl ether) level. All energy values are given in kcal·mol^{-1}.

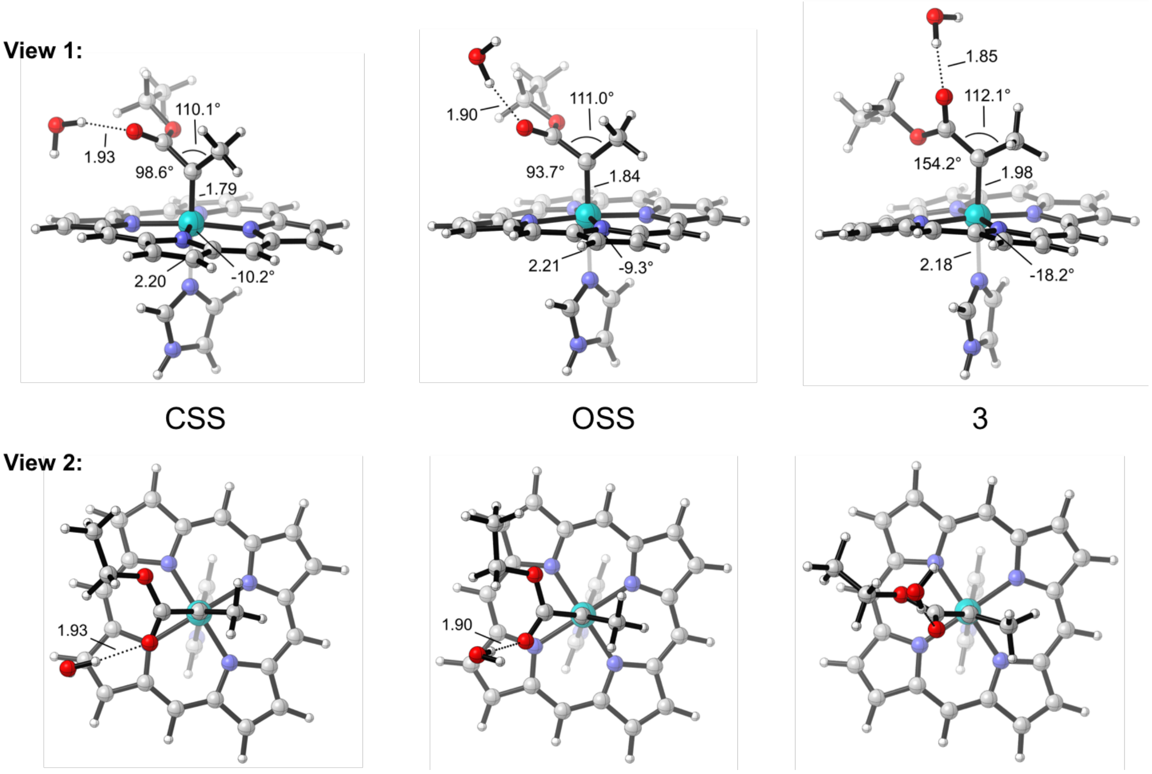

Relative stabilities of different electronic states:

IPC 1 – Water electronic state	ΔE	Δ(E+ZPE)	ΔH	ΔG	ΔG-qh
closed-shell singlet (CSS)	0.0	0.0	0.0	0.1	**0.0**
open-shell singlet (OSS)	1.8	1.3	1.6	0.0	**1.0**
triplet (3)	10.5	10.2	10.4	8.8	**9.6**

Energies in kcal·mol^{-1}.

All energy values discussed in the manuscript correspond to the quasi-harmonic corrected Gibbs energies (ΔG-qh) at (U)B3LYP-D3(BJ)/Def2TZVP/PCM(diethyl ether)//(U)B3LYP/6-31G(d)+SDD(Fe)/PCM(diethyl ether) level, if not otherwise noted.

DFT calculations on IPC **1**-water model showed that CSS (closed-shell singlet) electronic state is lower in energy than the open-shell singlet (OSS) by 1 kcal·mol^{-1}, which corresponds to the opposite relative stability to the one found in the IPC **1** model in Figure S5. Both singlet states are still significantly more stable that the triplet state, similar to the IPC **1** model. Although the small energy difference between OSS and CSS is still within method error, it is significant that the relative stability of the two states has been reversed due to the presence of the H-bonding water molecule. In addition, no significant changes in the geometries are observed when comparing the IPC **1**-water optimized structures to the structures obtained for IPC **1** reported in Figure S5.

The stabilization of IPC has been analyzed in terms of the hypothetical equilibrium described in Scheme 1, where the isolated IPC **1** and a water molecule are brought together from infinite separation:

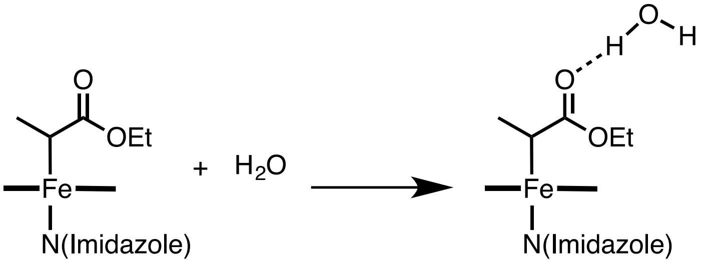

Scheme 1. IPC **1** stabilization by H-bonding water molecule

IPC 1 stabilization by H-bonding water molecule:

electronic state	ΔE	Δ(E+ZPE)	ΔH	ΔG	ΔG-qh
closed-shell singlet (CSS)	-9.0	-6.7	**-7.2**	2.2	2.6
open-shell singlet (OSS)	-6.5	-4.5	**-4.7**	3.5	4.6
triplet (3)	-8.6	-6.1	**-6.6**	2.9	3.4

Energies in kcal·mol^{-1}

All energy values discussed in the manuscript about IPC **1** stabilization by H-bonding water molecule correspond to the enthalpy (ΔH) at (U)B3LYP-D3(BJ)/Def2TZVP/PCM(diethyl ether)//(U)B3LYP/6-31G(d)+SDD(Fe)/PCM(diethyl ether) level, if not otherwise noted.

Since this is a bimolecular-to-unimolecular process, where two molecules (IPC **1** and water) are brought together to generate a complex that is entropically unfavorable, we focused on analyzing the stabilization due to H-bonding in terms of the enthalpy (ΔH) of the process. Based on this, DFT calculations showed that H-bonding stabilization is greater in the CSS state than in the OSS and triplet by 2.5 and 0.6 kcal·mol^{-1}, respectively.

Taken together, these results indicate that the presence of a H-bonding water molecule greatly stabilizes IPC **1**, and that stabilization is the largest in the closed-shell singlet electronic state.

Figure S10. QM/MM modelling of the full IPC *Rma* TDE. QM/MM optimized structures of IPC **1** *Rma* TDE from a representative snapshot of the preferred orientation of the carbene obtained from MD simulations at (U)B3LYP/Def2TZVP:AmberFF14Sb//(U)B3LYP/6-31G(d)+SDD:AmberFF14Sb level (see computational details for expanded description). QM-region atoms are shown in ball-and-stick format. For more clear comparisons, only the QM-region atoms are shown in the optimized structures. Key distances, angles and dihedrals are given in angstrom (Å) and degrees (°). A table containing the relative stabilities of the different optimized species in terms of their electronic energy (ΔE), zero-point corrected energy (Δ(E+ZPE)), enthalpy (ΔH), Gibbs energy (ΔG), and quasi-harmonic corrected Gibbs energy (ΔG-qh) is reported. All energy values are given in kcal·mol^{-1}.

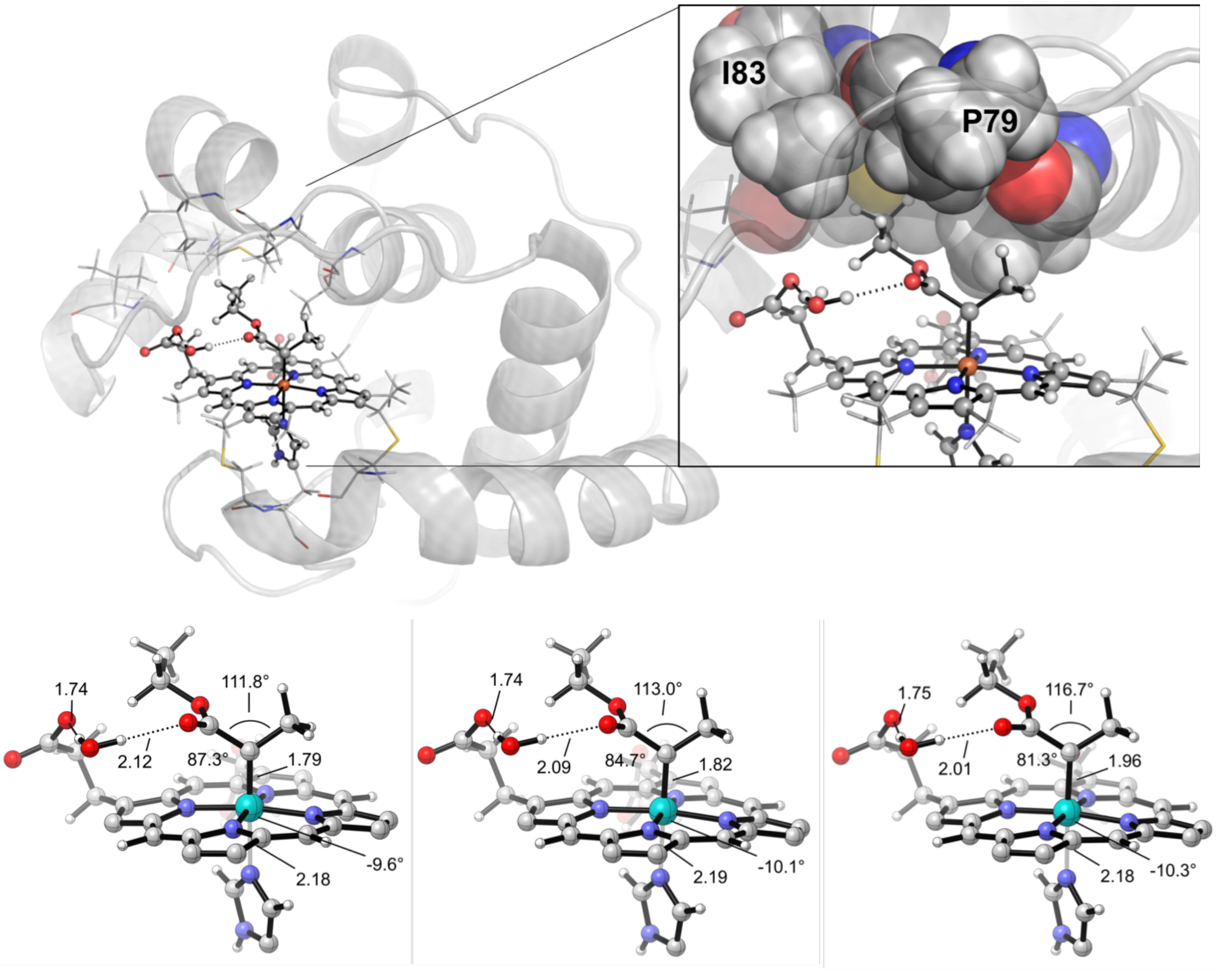

CSS OSS 3

IPC 1 electronic state	ΔE	Δ(E+ZPE)	ΔH	ΔG	ΔG-qh
closed-shell singlet (CSS)	1.0	1.1	1.1	1.1	**1.1**
open-shell singlet (OSS)	0.0	0.0	0.0	0.0	**0.0**
triplet (3)	13.9	13.5	13.7	12.4	**12.8**

Energies in kcal·mol^{-1}

All energy values discussed in the manuscript correspond to the quasi-harmonic corrected Gibbs energies (ΔG-qh) at (U)B3LYP/Def2TZVP//(U)B3LYP/6-31G(d)+SDD level, if not otherwise noted.

QM/MM calculations in the framework of the ONIOM approach were carried out to investigate the impact of the protein scaffold on the geometry and electronic states of IPC **1**. We started from a representative snapshot of the most populated cluster characterized from MD simulations (obtained from replica 0, see Figure S7.B), in which the carbene is in its preferred orientation, i.e. the crystal structure-like conformation for IPC **1**. Taking this structure from MD, IPC **1** was optimized in three different electronic states: the closed-shell and open-shell singlet (CSS and OSS, respectively), and triplet (3) states. QM/MM calculations showed that OSS is lower in energy than CSS by only 1.1 kcal·mol^{-1}, the same energy difference found for the truncated DFT model calculations (Figure S5). This very small energy difference is within the method error, and does not allow to us to unambiguously assign an electronic ground state. QM/MM calculations also revealed that the triplet state is 12.8 and 11.7 kcal·mol^{-1} higher in energy than the OSS and CSS, respectively. This represents a 3 kcal·mol^{-1} destabilization of the triplet state with respect both singlet states as compared to the relative stabilities computed for the truncated DFT model (Figure S5).

The large destabilization of the radical triplet state comes from the conformational restraints imposed by the protein environment to the IPC. First, the steric clashes between the carbene ester group and P79 and I83 residues do not allow the ester group to rotate and adopt its triplet-preferred conformation to stabilize the carbene radical character associated with the triple state (see discussion in Figure S5 and QM/MM optimized structures). Second, the covalent linkage of the heme group to C45 and C48 prevents porphyrin ruffling that was found to be necessary for stabilizing IPC **1** triplet state (see discussion in Figure S5 and ruffling values in Table S2).

QM/MM optimized geometries, apart from the already-described different orientation of the ester in the triplet state, are very similar to those optimized in the truncated DFT model (Figure S5). The bridging water molecule between the carbene and heme carboxyl group is strongly hydrogen bonded in all three optimized QM/MM geometries, confirming its importance in stabilizing the carbene conformation in the *Rma* TDE active site.

As a whole, QM/MM calculations revealed a destabilization of the radical triplet state with respect to the singlet states due to conformational restraints imposed by the protein environment to the IPC structure, and further reinforced the role played by the bridging water molecule in stabilizing the catalytically relevant conformation adopted by the IPC.

Figure S11. GC Standard curve for ethyl 2-(dimethylphenylsilyl)propanoate product.

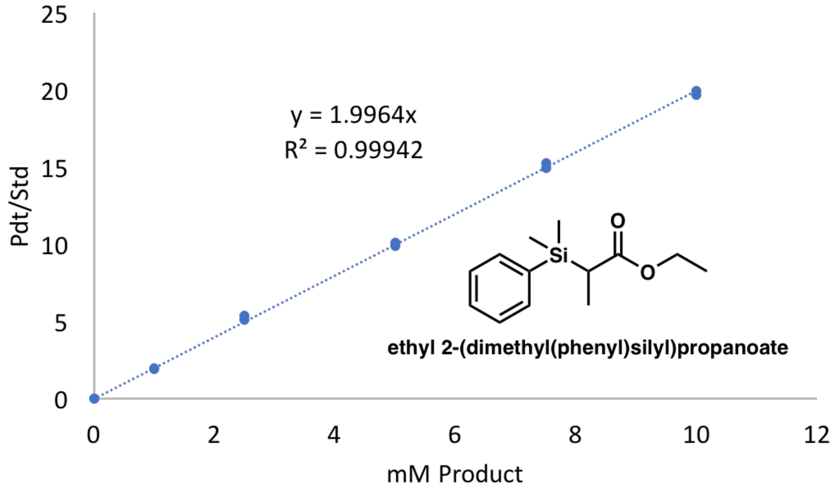

Total turnover for reactions with 2 μM *Rma* TDE was determined to be 828 +/- 15 TTN.
P dt / std = ratio of product to internal standard (see section (II)F).

Figure S12. ^{1}H NMR for Ethyl 2-(dimethylphenylsilyl)propanoate product. ^{1}H NMR (400 MHz, $CDCl_3$) δ 7.55-7.46 (m, 2H), 7.43-7.32 (m, 3H), 4.02 (q, *J* = 7.1 Hz, 2H), 2.25 (q, *J* = 7.1 Hz, 1H), 1.17-1.11 (m, 6H), 0.37 (d, *J* = 0.6 Hz, 6H).

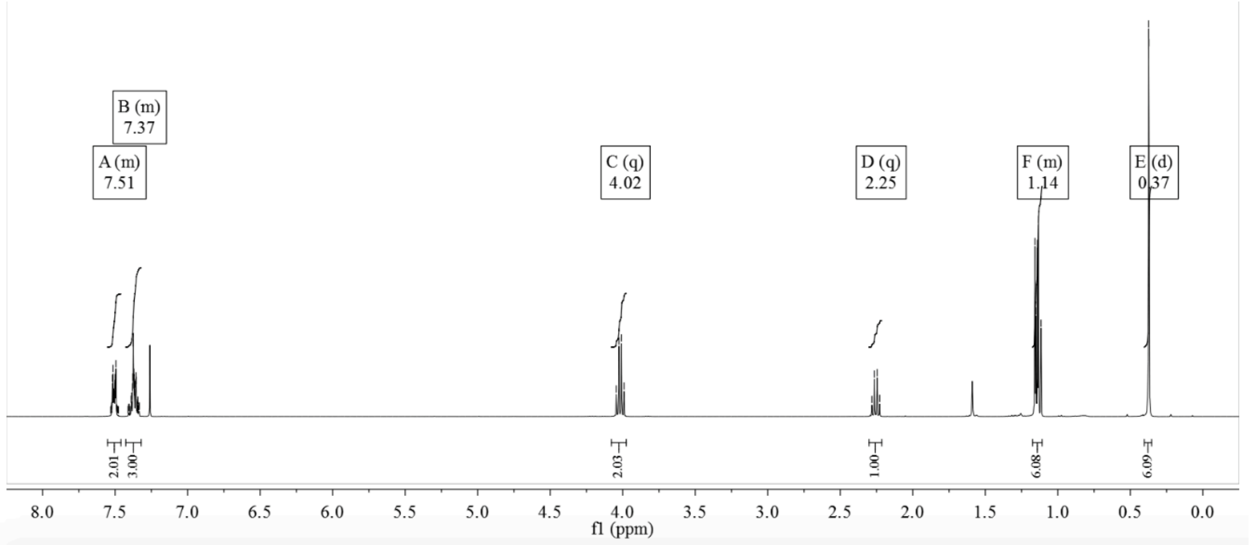

Figure S13. Separation of ethyl 2-(dimethylphenylsilyl)propanoate.

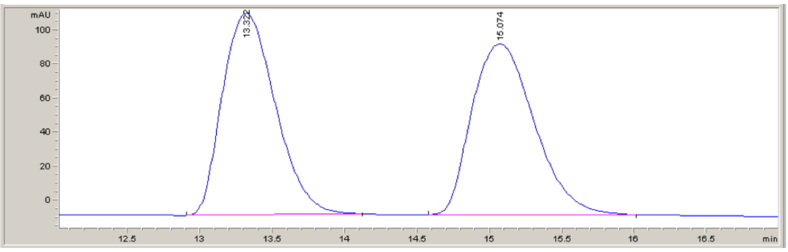

Retention time (min)	Area (mAU*s)	Area (%)
13.322	3015.8	50.01
15.074	3014.6	49.99

Enantiomeric excess (% ee)	0.02 %

A. Separation of racemic ethyl 2-(dimethylphenylsilyl)propanoate. A representative chiral HPLC trace of chemically-synthesized ethyl 2-(dimethylphenylsilyl)propanoate shows that the product is racemic, as expected.

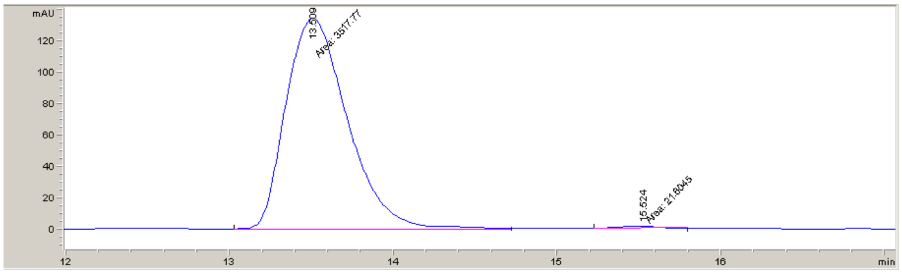

Retention time (min)	Area (mAU*s)	Area(%)
13.351	3517.8	99.39
15.524	21.6	0.61

Enantiomeric excess (%ee)	98.78%

B. Separation of enzymatically-produced ethyl 2-(dimethylphenylsilyl)propanoate. A representative chiral HPLC trace of ethyl 2-(dimethylphenylsilyl)propanoate produced from a reaction catalyzed by *Rma* TDE shows that the enzyme produces product with 99% *ee*. The product was assigned as having the *R* absolute configuration based on comparison of retention times to the literature.[4,69]

Table S3. DFT / QM/MM optimized geometries. Energies and thermochemistry parameters (at T = 298.15 K and P = 1 atm) of all computationally characterized stationary points: Electronic energies (E), electronic energies from high level single point calculations (E (SP)), Zero point energy (ZPE), enthalpy (H), entropic term (T·S), quasi-harmonic corrected entropic term (T·S-qh), free energy (G(T)), quasi-harmonic corrected free energy (G(T)- qh). All energies are given in a.u.

Structure	**E**	**ZPE**	**H**	**T·S**	**T·S-qh**	**G(T)**	**G(T)-qh**	**E (SP)**
IPC **1** - CSS DFT truncated model	-1684.343369	0.473668	-1683.837247	0.094828	0.088519	-1683.932076	-1683.925766	-2824.95294655
IPC **1** - OSS DFT truncated model	-1684.346119	0.473392	-1683.840144	0.095579	0.088700	-1683.935723	-1683.928844	-2824.95422900
IPC **1** - 3 DFT truncated model	-1684.331005	0.472852	-1683.825406	0.097498	0.090092	-1683.922903	-1683.915497	-2824.93686800
IPC **1** - water - CSS DFT truncated model	-1760.769157	0.498466	-1760.235230	0.101204	0.094370	-1760.336434	-1760.329600	-2901.43551956
IPC **1** - water - OSS DFT truncated model	-1760.769368	0.497683	-1760.235706	0.103987	0.095269	-1760.339693	-1760.330975	-2901.43271300
IPC **1** - water - 3 DFT truncated model	-1760.754609	0.497948	-1760.220928	0.103899	0.095696	-1760.324826	-1760.316620	-2901.41872400
(Fe,N)-bridged IPC **1** - CSS DFT truncated model	-1684.317678	0.474653	-1683.811316	0.092427	0.086484	-1683.903743	-1683.897801	-2824.92362120
(Fe,N)-bridged IPC **1** - OSS DFT truncated model	-1684.322762	0.474606	-1683.816449	0.092284	0.086491	-1683.908732	-1683.90294	-2824.93079848
(Fe,N)-bridged IPC **1** - 3 DFT truncated model	-1684.325620	0.473901	-1683.819674	0.094808	0.088471	-1683.914483	-1683.908145	-2824.93626367
(Fe,N)-bridged IPC **1** - 5 DFT truncated model	-1684.328791	0.472107	-1683.824072	0.096878	0.090288	-1683.92095	-1683.91436	-2824.93133613
TS Si-H insertion - CSS	-2285.914894	0.648074	-2285.223626	0.116937	0.108566	-2285.340563	-2285.332192	-3426.74469549
TS Si-H insertion - 3	-2285.897188	0.645349	-2285.207539	0.123159	0.111825	-2285.330699	-2285.319365	-3426.71997476
QM/MM IPC **1** - CSS	-2330.143247	8.891718	-2320.682274	1.145116	1.071216	-2321.827390	-2321.753489	-3470.90714600
QM/MM IPC **1** - OSS	-2330.145407	8.891570	-2320.684551	1.145180	1.071243	-2321.829732	-2321.755795	-3470.90878500
QM/MM IPC **1** - 3	-2330.123448	8.891040	-2320.662902	1.147209	1.072564	-2321.810111	-2321.735465	-3470.88670600

Cartesian coordinates of all optimized stationary points in xyz format:

DFT optimized truncated model structures:

IPC 1 closed-shell singlet DFT truncated model

Fe	-0.29198100	0.01077800	-0.09863600
N	1.29834000	0.68867100	0.95872700
N	0.13789500	-1.87757600	0.48060000
N	-0.84213900	1.92464700	-0.48976800
N	-1.99915100	-0.64497100	-0.97053000
C	1.73703500	1.98607500	1.03402300
C	-0.51976600	-3.01860000	0.09860500
C	2.18569000	-0.05940400	1.68679300
C	1.17882100	-2.28353100	1.27364700
C	-0.11588400	3.05674600	-0.21708200
C	-2.37086800	-1.95227000	-1.15630200
C	-1.99051900	2.34574000	-1.10969100
C	-2.99281000	0.11893900	-1.52654700
C	2.93931500	2.06040400	1.83639500
C	0.12571100	-4.18209400	0.66900900
C	3.21416900	0.79085400	2.24758800
C	1.17521500	-3.72520800	1.40500500
C	-0.82319600	4.22848100	-0.68780300
C	-3.63399400	-2.01689000	-1.86037000
C	-1.99020600	3.78765800	-1.23458300
C	-4.02408300	-0.73135100	-2.08261300
H	3.47984200	2.97289900	2.05644100
H	-0.20160500	-5.20387600	0.52133000
H	4.02829800	0.44532000	2.87293600
H	1.89157400	-4.29399200	1.98497700
H	-0.46443200	5.24612700	-0.59357600
H	-4.14502500	-2.93322900	-2.12911700
H	-2.78591300	4.36849800	-1.68474900
H	-4.92034400	-0.37365900	-2.57446700
C	1.09591600	3.08748800	0.47052800
C	-1.67218000	-3.06076600	-0.68241700
C	-3.00245400	1.51104500	-1.57976700
C	2.12717000	-1.44187800	1.84872300
H	1.55855400	4.05946700	0.61715600
H	-2.08635500	-4.04034300	-0.90350400
H	-3.85726800	1.98456800	-2.05429100
H	2.90098900	-1.90507500	2.45433900
C	-1.43640200	1.20722900	2.60784600
C	-2.35535200	-0.72231900	2.29304100
C	-2.87331300	-0.23992100	3.46636200
N	-1.46077400	0.18799400	1.76685100
N	-2.27657800	0.99084700	3.65167800
H	-3.58836100	-0.64387100	4.16597600
H	-2.56144500	-1.65568700	1.79241500
H	-0.83821900	2.09863400	2.49822200
H	-2.43367800	1.62179600	4.42495400
C	0.63845100	-0.11678600	-1.62658500
C	1.97994500	-0.77304300	-1.71425700
O	2.11833900	-1.95771700	-1.96613000
O	3.00009700	0.08437500	-1.54049200
C	4.33539900	-0.48151700	-1.60691100
H	4.46661200	-0.95948800	-2.58257300
H	4.42078000	-1.25283100	-0.83574300
C	5.32037500	0.65067100	-1.38821500
H	6.34350300	0.26095800	-1.42702700
H	5.21445700	1.41759100	-2.16254800
H	5.16151400	1.11679000	-0.41080500
C	0.19914900	0.33518300	-2.98747400
H	0.92256800	1.06601400	-3.38300200
H	0.22257500	-0.51948200	-3.68116300
H	-0.79573700	0.77649600	-2.99327400

IPC 1 open-shell singlet DFT truncated model

Fe	-0.30088100	0.01234900	-0.08738400
N	1.28049200	0.70708600	0.96635800
N	0.15132500	-1.86766500	0.49482700
N	-0.86363700	1.91461200	-0.49900800
N	-1.99111600	-0.66274900	-0.97119500
C	1.71057800	2.00831700	1.02933800
C	-0.48782700	-3.01713100	0.10572100
C	2.17347900	-0.02791900	1.70222900
C	1.19334000	-2.26164900	1.29372000
C	-0.14409400	3.05365100	-0.23689300
C	-2.34301900	-1.97524900	-1.16064100
C	-2.01198900	2.32326900	-1.12882100
C	-2.98979700	0.08747700	-1.53850200
C	2.91054100	2.09825300	1.83223300
C	0.16971400	-4.17192100	0.67800600
C	3.19374900	0.83474700	2.25638500
C	1.20794400	-3.70240200	1.42237600
C	-0.85559000	4.21547200	-0.72334500
C	-3.59779200	-2.05670900	-1.87619800
C	-2.01868000	3.76271300	-1.26908900
C	-4.00355300	-0.77656400	-2.10265900
H	3.44501600	3.01642800	2.04285600
H	-0.14195900	-5.19773500	0.52500700
H	4.01008500	0.50069200	2.88492600
H	1.92873200	-4.26252900	2.00510900
H	-0.50163400	5.23570700	-0.64038800
H	-4.09293000	-2.98005600	-2.15038400
H	-2.81513000	4.33411100	-1.72968000
H	-4.89920000	-0.43121500	-2.60416800
C	1.06443500	3.10020400	0.45456600
C	-1.63443300	-3.07483100	-0.68198800
C	-3.01522600	1.47848700	-1.59773000
C	2.12843100	-1.40915800	1.87312400
H	1.52071000	4.07634300	0.59210300
H	-2.03344000	-4.05955500	-0.90728600
H	-3.87097900	1.94116800	-2.08084600
H	2.90462600	-1.86170500	2.48343000
C	-1.47100800	1.20975000	2.60878700
C	-2.36578400	-0.73316400	2.29982700
C	-2.89343500	-0.25091700	3.46875100
N	-1.48052000	0.18579900	1.77296600
N	-2.31210300	0.98771100	3.65010400
H	-3.60611600	-0.65998600	4.16775000
H	-2.55882200	-1.67130000	1.80290100
H	-0.88311800	2.10769900	2.49681600
H	-2.47954300	1.62032400	4.41993500
C	0.66051900	-0.12296100	-1.64500800
C	2.00013600	-0.77482000	-1.71021800
O	2.16795800	-1.95965100	-1.94883400
O	3.01781200	0.09346300	-1.53073600
C	4.35426900	-0.46344500	-1.58673500
H	4.49675900	-0.94510700	-2.55932700
H	4.44270900	-1.23243000	-0.81308500
C	5.33262800	0.67491300	-1.36668400
H	6.35865200	0.29199900	-1.39899100
H	5.22581900	1.43910700	-2.14370700
H	5.16624100	1.14385900	-0.39177100
C	0.21157300	0.31812300	-3.00998500
H	0.92769500	1.04277000	-3.42981900
H	0.20678900	-0.54177600	-3.69829000
H	-0.77998500	0.76884400	-3.00633200

IPC 1 triplet DFT truncated model

Fe	-0.28017000	-0.00047100	-0.01769300
N	0.49735800	0.75824500	1.66305900
N	0.11923500	-1.86386200	0.58449900
N	-0.84076700	1.86831800	-0.55237100
N	-1.21183600	-0.76659100	-1.63919900
C	0.71731200	2.08081500	1.96544800
C	-0.01309700	-3.02565700	-0.13585000
C	0.94915200	0.03728400	2.73801300
C	0.61967200	-2.22492200	1.80790700
C	-0.45849600	3.05162100	0.02886900

C	-1.18379300	-2.06590600	-2.07955900
C	-1.65377600	2.20120600	-1.60667100
C	-1.97582200	-0.06999300	-2.54175800
C	1.34075000	2.19576200	3.26339100
C	0.43129400	-4.15229900	0.65193400
C	1.46478400	0.92946000	3.75084200
C	0.80285900	-3.65732400	1.86523600
C	-1.03916200	4.16542400	-0.68341800
C	-1.94173000	-2.19321800	-3.30230900
C	-1.79607600	3.63680500	-1.68663200
C	-2.44899000	-0.95870600	-3.57869300
H	1.62160200	3.13060100	3.73223300
H	0.43227400	-5.18041800	0.31215900
H	1.87860100	0.61026600	4.69932300
H	1.18323100	-4.19526400	2.72467600
H	-0.89188000	5.20712400	-0.42679700
H	-2.07424800	-3.11575000	-3.85357300
H	-2.39050800	4.15694800	-2.42755900
H	-3.07650700	-0.65835700	-4.40866600
C	0.30758800	3.15894200	1.18699000
C	-0.58456700	-3.12360100	-1.40049400
C	-2.21497400	1.30213100	-2.51066000
C	0.96134500	-1.35012800	2.83301500
H	0.54066000	4.15670400	1.54627000
H	-0.63232800	-4.10765200	-1.85682500
H	-2.84002500	1.71448900	-3.29717700
H	1.34289700	-1.78373900	3.75256800
C	-2.73522300	0.74464400	1.81576500
C	-3.06820100	-1.24074900	1.02162400
C	-4.15007400	-0.95710300	1.81170600
N	-2.19350800	-0.17282500	1.03211700
N	-3.92025900	0.31089000	2.30853800
H	-5.03574000	-1.52050900	2.06056900
H	-2.85633300	-2.13086400	0.44990900
H	-2.30841000	1.70922700	2.04306500
H	-4.52567700	0.82830400	2.93061100
C	1.38344500	0.21899000	-1.05159300
C	2.68682000	-0.14437700	-0.52165400
O	2.94041900	-0.77194800	0.50680900
O	3.72261500	0.29733600	-1.32761100
C	5.04535100	-0.04076700	-0.88814600
H	5.13670900	-1.13035800	-0.80900900
H	5.21514500	0.37240400	0.11286000
C	6.02618100	0.52879500	-1.89954400
H	7.05338800	0.29245300	-1.59977800
H	5.85193300	0.10561000	-2.89468700
H	5.92931700	1.61770100	-1.96739500
C	1.37679700	0.88300000	-2.40287000
H	1.72990300	1.92451400	-2.32879700
H	2.06256000	0.37932800	-3.09637000
H	0.38580600	0.90637600	-2.85301700

IPC 1 - water closed-shell singlet DFT truncated model

Fe	0.43819	-0.01401	-0.09854
N	1.85491	-1.27614	-0.81252
N	-0.52550	-1.58210	0.74242
N	1.52945	1.56296	-0.74428
N	-0.86039	1.25403	0.80454
C	3.03054	-0.93616	-1.43072
C	-1.60612	-1.53531	1.58373
C	1.81070	-2.64676	-0.80126
C	-0.25588	-2.91120	0.53853
C	2.73760	1.52360	-1.39022
C	-1.88877	0.92240	1.64809
C	1.17309	2.88727	-0.67272
C	-0.88319	2.62018	0.68502
C	3.75246	-2.12871	-1.82240
C	-2.02983	-2.87634	1.92829
C	2.99049	-3.19048	-1.44107
C	-1.19900	-3.73041	1.26983
C	3.15976	2.86376	-1.73866
C	-2.58452	2.11603	2.07864
C	2.18565	3.70870	-1.30126
C	-1.96551	3.17085	1.47126
H	4.71256	-2.13268	-2.32359
H	-2.85451	-3.11234	2.58965
H	3.19754	-4.24689	-1.55987
H	-1.19850	-4.81340	1.27903
H	4.08251	3.10623	-2.25123
H	-3.42310	2.12985	2.76441
H	2.14424	4.78817	-1.37833
H	-2.19447	4.22609	1.55589
C	3.45223	0.36539	-1.69183
C	-2.23368	-0.37408	2.02438
C	0.04154	3.38169	-0.02845
C	0.81197	-3.41231	-0.20349
H	4.40289	0.48762	-2.20297
H	-3.07901	-0.48856	2.69678
H	-0.10658	4.45765	-0.04155
H	0.90521	-4.49234	-0.27243
C	1.95396	1.17241	2.41966
C	2.18068	-0.97602	2.45368
C	2.84801	-0.50425	3.55344
N	1.62742	0.07783	1.75432
N	2.69315	0.86664	3.51595
H	3.40213	-0.99963	4.33538
H	2.06006	-1.99411	2.11737
H	1.68123	2.17996	2.14604
H	3.06214	1.52892	4.18375
C	-0.49915	-0.06826	-1.62808
C	-1.98199	0.11033	-1.67300
O	-2.48007	1.19325	-1.96215
O	-2.67705	-0.99783	-1.41921
C	-4.13083	-0.89982	-1.48703
H	-4.40560	-0.60370	-2.50455
H	-4.45786	-0.11228	-0.80381
C	-4.69191	-2.25929	-1.12089
H	-5.78620	-2.22250	-1.15302
H	-4.35177	-3.02757	-1.82296
H	-4.38168	-2.54913	-0.11227
C	0.04805	-0.18182	-3.01983
H	-0.22827	-1.17001	-3.42417
H	-0.42039	0.56187	-3.67991
H	1.13114	-0.08310	-3.06269
H	-4.03010	2.05153	-1.20336
O	-4.68211	2.39870	-0.56571
H	-4.13394	2.55084	0.22201

IPC 1 - water open-shell singlet DFT truncated model

Fe	0.45854	0.00786	-0.05974
N	1.48883	-1.40440	-1.08050
N	-0.58274	-1.43655	0.89621
N	1.64327	1.43449	-0.86970
N	-0.43346	1.40071	1.10215
C	2.55906	-1.21142	-1.91696
C	-1.48968	-1.27328	1.91073
C	1.22445	-2.75099	-1.10122
C	-0.56559	-2.77763	0.60932
C	2.69213	1.25208	-1.73522
C	-1.36341	1.18992	2.08823
C	1.52474	2.78972	-0.69076
C	-0.27489	2.76064	1.01058
C	2.98340	-2.47267	-2.48332
C	-2.05603	-2.55060	2.28522
C	2.14948	-3.42699	-1.98430
C	-1.48853	-3.48364	1.47101
C	3.25393	2.52997	-2.11368
C	-1.79891	2.45261	2.64239
C	2.52393	3.48457	-1.47266
C	-1.12977	3.42764	1.96775
H	3.81095	-2.59278	-3.17154
H	-2.78843	-2.69476	3.06991
H	2.15339	-4.49307	-2.17496
H	-1.65621	-4.55342	1.45061

H	4.09386	2.66027	-2.78484
H	-2.52624	2.55952	3.43760
H	2.64236	4.56054	-1.50647
H	-1.19106	4.50115	2.09679
C	3.13651	0.02117	-2.21107
C	-1.84634	-0.05474	2.48205
C	0.61865	3.41254	0.16446
C	0.25349	-3.39129	-0.33487
H	3.98004	0.02609	-2.89523
H	-2.58357	-0.07422	3.27939
H	0.63892	4.49772	0.20464
H	0.15868	-4.46707	-0.45064
C	2.46530	0.78515	2.26846
C	2.60409	-1.34893	1.95396
C	3.48230	-1.05314	2.96310
N	1.97581	-0.19533	1.52908
N	3.38137	0.31059	3.14939
H	4.14931	-1.66631	3.54867
H	2.38012	-2.30468	1.50620
H	2.18873	1.82565	2.19677
H	3.89506	0.86204	3.82234
C	-0.78867	0.18119	-1.40232
C	-2.23958	0.37434	-1.12695
O	-2.76212	1.48304	-1.06538
O	-2.91604	-0.77529	-1.00199
C	-4.33363	-0.69215	-0.68625
H	-4.82083	-0.01222	-1.38920
H	-4.42832	-0.26734	0.31843
C	-4.89572	-2.09871	-0.75849
H	-5.96221	-2.08049	-0.50888
H	-4.78566	-2.51299	-1.76618
H	-4.38351	-2.75910	-0.05167
C	-0.50890	0.23160	-2.87866
H	-1.01056	-0.60738	-3.38796
H	-0.92932	1.15160	-3.31367
H	0.55480	0.18839	-3.10872
H	-4.50160	2.14675	-1.44407
O	-5.36120	2.39249	-1.83936
H	-5.14812	2.49152	-2.77982

IPC 1 - water triplet DFT truncated model

Fe	0.43970400	-0.00116800	-0.03718100
N	1.41041600	-1.06112600	-1.45472600
N	-0.52508900	-1.67109600	0.49057500
N	1.55416300	1.63043400	-0.45849700
N	-0.40125600	1.01336400	1.46795800
C	2.48023100	-0.63071700	-2.19909300
C	-1.27940500	-1.84099500	1.62151300
C	1.11806700	-2.32700300	-1.89525000
C	-0.57577000	-2.86350600	-0.18971600
C	2.59923300	1.69119800	-1.34515500
C	-1.18617800	0.48139900	2.45851000
C	1.38592900	2.90217100	0.02880600
C	-0.32721600	2.36395600	1.71664300
C	2.87794300	-1.65983300	-3.13278700
C	-1.81980900	-3.18117900	1.66024900
C	2.02000000	-2.70440800	-2.95808900
C	-1.40425000	-3.80762100	0.52405800
C	3.11516300	3.03963600	-1.40838600
C	-1.62382700	1.52527300	3.35660800
C	2.34955900	3.79518800	-0.57096900
C	-1.11015700	2.69581500	2.88358100
H	3.70004000	-1.57313400	-3.83227100
H	-2.44599800	-3.57024800	2.45347400
H	1.99935300	-3.65441500	-3.47714100
H	-1.60852200	-4.81947900	0.19714000
H	3.94537800	3.35355100	-2.02880300
H	-2.25230000	1.36817100	4.22443700
H	2.42762400	4.85364000	-0.35644200
H	-1.22277000	3.69417200	3.28730800
C	3.06035800	0.63362500	-2.12532100
C	-1.55170200	-0.85697000	2.56633200
C	0.47466200	3.26181700	1.01903100
C	0.15389200	-3.16194700	-1.33585400
H	3.90133500	0.83234000	-2.78298600
H	-2.16115400	-1.14006200	3.41928300
H	0.44257500	4.30458100	1.31952500
H	0.02309300	-4.14613900	-1.77514000
C	2.64866600	0.19028500	2.19582400
C	2.56170900	-1.86134100	1.51101000
C	3.52895800	-1.82029100	2.47925100
N	2.02036300	-0.60240200	1.34325000
N	3.56970300	-0.50658800	2.90326200
H	4.17394100	-2.57883000	2.89429500
H	2.21787100	-2.70033100	0.92634100
H	2.46723100	1.24609900	2.32414600
H	4.17843400	-0.12698400	3.61512500
C	-0.89017000	0.61091100	-1.36684600
C	-2.31926300	0.79597800	-1.16413100
O	-2.99315100	1.59139700	-1.84463800
O	-2.90645800	0.04393500	-0.20012000
C	-4.32409400	0.25424100	-0.01526100
H	-4.83100100	0.17287100	-0.98045700
H	-4.48323400	1.27377600	0.35508500
C	-4.83872800	-0.78009500	0.96897000
H	-5.92072400	-0.65694300	1.09190800
H	-4.64536000	-1.79487800	0.60600700
H	-4.36336500	-0.66846700	1.94761200
C	-0.42326300	1.19238300	-2.67691200
H	0.48134700	0.70607100	-3.04271500
H	-1.20274300	1.11996400	-3.44425000
H	-0.19008900	2.26359100	-2.56979200
H	-4.59298400	1.36433000	-2.75313300
O	-5.37877000	1.07005200	-3.25954200
H	-5.03460800	0.32734900	-3.77877700

TS Si-H carbene insertion closed-shell singlet

Fe	0.78460	0.50830	0.07990
N	2.12590	-0.60370	1.14410
N	-0.43880	0.52960	1.68110
N	2.13260	0.67550	-1.43760
N	-0.45340	1.77230	-0.91180
C	3.38860	-0.96480	0.74790
C	-1.61130	1.23390	1.79980
C	1.96900	-1.10050	2.41280
C	-0.24080	-0.08790	2.89150
C	3.39150	0.13280	-1.47860
C	-1.64740	2.26680	-0.45570
C	1.97370	1.36120	-2.61530
C	-0.27260	2.30800	-2.16220
C	4.03950	-1.73500	1.78780
C	-2.17150	1.05490	3.12290
C	3.15510	-1.82240	2.82090
C	-1.32060	0.23360	3.80040
C	4.04320	0.47400	-2.72650
C	-2.25560	3.11760	-1.45800
C	3.16160	1.23250	-3.43440
C	-1.40170	3.14290	-2.51840
H	5.04330	-2.13750	1.72350
H	-3.09060	1.51010	3.47140
H	3.28290	-2.31250	3.77850
H	-1.39790	-0.12560	4.81960
H	5.04470	0.16840	-3.00430
H	-3.20560	3.62510	-1.34380
H	3.28970	1.68080	-4.41220
H	-1.50410	3.67850	-3.45450
C	3.97850	-0.62580	-0.46850
C	-2.18560	2.02290	0.80510
C	0.84970	2.10930	-2.96460
C	0.86020	-0.87440	3.22570
H	4.99170	-0.97840	-0.64180
H	-3.13490	2.49650	1.03770
H	0.86260	2.60180	-3.93310
H	0.87450	-1.31120	4.22050
C	2.16880	2.39260	2.16790
C	2.02860	3.45170	0.28980

C	2.62970	4.31280	1.16940
N	1.74500	2.25680	0.92250
N	2.71050	3.62170	2.36160
H	2.99690	5.32160	1.06270
H	1.78180	3.60530	-0.74880
H	2.10080	1.64240	2.94010
H	3.10320	3.96440	3.22690
C	0.02280	-1.04950	-0.78740
C	0.57990	-2.40160	-0.41920
O	0.23770	-3.11880	0.50730
O	1.55350	-2.75270	-1.28870
C	2.26060	-3.98260	-1.00100
H	1.53350	-4.79610	-0.91840
H	2.76290	-3.87530	-0.03500
C	3.24770	-4.21580	-2.12940
H	3.80840	-5.13870	-1.94420
H	2.73030	-4.31410	-3.08950
H	3.95790	-3.38620	-2.20160
C	-0.44340	-1.01500	-2.23250
H	-0.86290	-1.96260	-2.58990
H	-1.16210	-0.21050	-2.39540
H	0.43500	-0.79490	-2.84970
Si	-2.71160	-2.07860	0.14430
C	-4.13490	-0.92320	-0.30040
C	-4.98820	-0.40230	0.69130
C	-4.40080	-0.57220	-1.63890
C	-6.06190	0.42870	0.36280
H	-4.81580	-0.64720	1.73610
C	-5.46680	0.26480	-1.97310
H	-3.76940	-0.95580	-2.43720
C	-6.30180	0.76640	-0.97110
H	-6.71010	0.81200	1.14690
H	-5.64830	0.52210	-3.01340
H	-7.13540	1.41440	-1.22910
H	-1.37150	-1.27440	-0.11660
C	-2.71870	-3.57460	-1.00790
H	-2.74630	-3.30010	-2.06750
H	-1.84010	-4.20250	-0.83300
H	-3.61380	-4.17480	-0.79960
C	-2.76070	-2.60660	1.94660
H	-1.87550	-3.21080	2.16420
H	-2.76340	-1.75130	2.62810
H	-3.65630	-3.21120	2.13870

TS Si-H carbene insertion triplet

Fe	-0.93053700	-0.52026400	0.04911100
N	-2.54479200	0.55838800	0.60705200
N	-0.16209400	-0.38486600	1.90838900
N	-1.80329400	-0.81451300	-1.75302200
N	0.60415200	-1.72427100	-0.46748700
C	-3.61098200	0.94374800	-0.17111400
C	1.02672400	-0.89905000	2.36197900
C	-2.78873600	1.05855800	1.86298400
C	-0.74330400	0.23630200	2.98369500
C	-2.96329500	-0.25222500	-2.22827700
C	1.71066600	-2.03762500	0.28246700
C	-1.32061300	-1.60514000	-2.76587200
C	0.75761900	-2.37855400	-1.66422500
C	-4.54217200	1.72246800	0.60967500
C	1.20063500	-0.59556300	3.76415200
C	-4.03570000	1.78618500	1.87405200
C	0.09860100	0.10530300	4.15077200
C	-3.21645600	-0.69520700	-3.57906400
C	2.59592400	-2.89778100	-0.46685400
C	-2.20095800	-1.54179800	-3.90947600
C	2.00029100	-3.11626300	-1.67219000
H	-5.46401000	2.14482200	0.22945900
H	2.05476600	-0.89428700	4.35907800
H	-4.45438700	2.27662000	2.74407200
H	-0.13757800	0.50594800	5.12870300
H	-4.06787400	-0.39578000	-4.17746800
H	3.54381200	-3.27329600	-0.10329600
H	-2.04474500	-2.07772700	-4.83750400
H	2.35646600	-3.71416700	-2.50190000
C	-3.80344900	0.58603900	-1.50157000
C	1.92116900	-1.64471100	1.60042800
C	-0.14090300	-2.34258000	-2.72652500
C	-1.96622500	0.89817500	2.97240800
H	-4.69448500	0.95806900	-1.99831700
H	2.83549900	-1.97748000	2.08163000
H	0.11298200	-2.91970900	-3.61076800
H	-2.29671000	1.34729900	3.90420300
C	-3.27052300	-2.61766200	0.50315000
C	-1.49424800	-3.37599300	1.47806200
C	-2.47695500	-4.30465100	1.69536900
N	-2.00042200	-2.32893300	0.73370300
N	-3.60056000	-3.80463800	1.06747500
H	-2.48327200	-5.24639300	2.22156100
H	-0.46517600	-3.38564400	1.80187600
H	-3.96363100	-2.00677400	-0.05428000
H	-4.51063200	-4.24264000	1.03268400
C	0.08144400	1.12433400	-0.63093600
C	-0.45121900	2.41648400	-0.12034300
O	-0.24269900	2.89703400	0.98661400
O	-1.19143400	3.09298300	-1.04980300
C	-1.74967500	4.35394100	-0.63053300
H	-0.93762900	5.02442400	-0.32882500
H	-2.38767700	4.18883500	0.24365400
C	-2.53801000	4.91688200	-1.79992700
H	-2.97807500	5.88182100	-1.52424400
H	-1.89231600	5.06920900	-2.67126400
H	-3.34769000	4.23692400	-2.08519800
C	0.41948300	1.15020200	-2.11492700
H	1.03686200	2.02478800	-2.36324000
H	0.97560200	0.25443100	-2.40423100
H	-0.47755800	1.20908400	-2.73979800
Si	2.97299700	1.85213300	0.33704000
C	4.40389900	0.74406900	-0.22650400
C	5.24976700	0.09360100	0.69406800
C	4.65171700	0.51813700	-1.59631800
C	6.29116500	-0.73715600	0.27215400
H	5.10017700	0.24243800	1.76104100
C	5.68898600	-0.31105100	-2.02629200
H	4.02301600	0.99758400	-2.34430300
C	6.51421500	-0.94309300	-1.09146000
H	6.93160200	-1.21927000	1.00733300
H	5.85578900	-0.46317800	-3.09010900
H	7.32420300	-1.58784200	-1.42321900
H	1.47355900	1.19279300	-0.02735000
C	3.05049700	3.48671900	-0.63404700
H	3.05740500	3.32881800	-1.71858000
H	2.18467600	4.11378900	-0.39213200
H	3.95659100	4.04937000	-0.37428600
C	3.13498600	2.24284400	2.18425900
H	2.29789900	2.88034400	2.48802400
H	3.09980100	1.34264900	2.80579600
H	4.07069900	2.77551900	2.39915600

(Fe,N)-bridged IPC 1 closed-shell singlet

Fe	0.48703	0.04361	-0.07056
N	1.70926	1.27343	-1.03210
N	1.63090	-1.53994	-0.59330
N	-0.68510	1.59093	0.49651
N	-1.13158	-1.30663	0.40866
C	1.61960	2.64139	-1.09604
C	1.40589	-2.86126	-0.32211
C	2.87118	0.94695	-1.68709
C	2.82603	-1.49683	-1.27408
C	-0.43830	2.92260	0.25791
C	-0.87244	-2.68375	0.67554
C	-1.85251	1.55151	1.20791
C	-2.13915	-0.91621	1.33873
C	2.73110	3.18931	-1.84632
C	2.50536	-3.67473	-0.80061
C	3.50926	2.13611	-2.21394
C	3.38551	-2.82609	-1.40025

C	-1.46333	3.74424	0.86507
C	-1.85030	-3.15155	1.60116
C	-2.33991	2.89207	1.46440
C	-2.60819	-2.08314	2.00667
H	2.88088	4.24290	-2.04716
H	2.56620	-4.75174	-0.70388
H	4.43241	2.14249	-2.78015
H	4.32097	-3.06097	-1.89280
H	-1.49735	4.82577	0.82020
H	-1.88345	-4.16372	1.98465
H	-3.24422	3.12828	2.01176
H	-3.37331	-2.07368	2.77292
C	0.62765	3.40894	-0.48773
C	0.25317	-3.38279	0.28679
C	-2.49663	0.38166	1.64051
C	3.39650	-0.34004	-1.79236
H	0.69374	4.48652	-0.61185
H	0.26335	-4.44312	0.52444
H	-3.34718	0.50472	2.30532
H	4.33650	-0.44706	-2.32708
C	1.13590	0.73898	2.85620
C	2.89892	-0.13770	1.96152
C	3.22022	0.12061	3.26743
N	1.59533	0.25234	1.71305
N	2.08608	0.67628	3.82213
H	4.12377	-0.03321	3.83645
H	3.50985	-0.57031	1.18535
H	0.14684	1.13850	3.01632
H	1.97682	0.98472	4.77789
C	-1.03384	-0.72435	-1.04354
C	-2.22870	0.10567	-1.46813
O	-2.14453	1.06510	-2.21385
O	-3.42998	-0.41313	-1.10622
C	-4.59983	0.30445	-1.55549
H	-4.59186	0.34704	-2.64934
H	-4.54852	1.33224	-1.18144
C	-5.81928	-0.42948	-1.02788
H	-6.73118	0.08396	-1.35203
H	-5.85074	-1.45722	-1.40463
H	-5.81282	-0.46324	0.06658
C	-0.97267	-1.80388	-2.13692
H	-1.00988	-1.28226	-3.09969
H	-0.05758	-2.39052	-2.12878
H	-1.83153	-2.49076	-2.09666

(Fe,N)-bridged IPC 1 open-shell singlet

Fe	0.49318	0.08585	-0.07898
N	1.55744	1.51182	-0.91197
N	1.83246	-1.30766	-0.71197
N	-0.83211	1.46930	0.62390
N	-0.92205	-1.40855	0.24262
C	1.27114	2.86982	-0.93555
C	1.75905	-2.67038	-0.54933
C	2.76044	1.37285	-1.58527
C	3.03991	-1.06917	-1.32158
C	-0.76203	2.83329	0.47041
C	-0.55999	-2.81532	0.34270
C	-1.94481	1.23635	1.39108
C	-1.99224	-1.23945	1.21626
C	2.29227	3.57916	-1.67547
C	2.95207	-3.29879	-1.02534
C	3.21059	2.66021	-2.07049
C	3.75581	-2.29568	-1.51444
C	-1.82829	3.47164	1.18074
C	-1.57187	-3.47662	1.11308
C	-2.56517	2.46760	1.76747
C	-2.41020	-2.54240	1.64037
H	2.29137	4.64865	-1.84635
H	3.14127	-4.36527	-1.01178
H	4.12131	2.81585	-2.63563
H	4.73227	-2.37998	-1.97497
H	-1.99752	4.54065	1.21939
H	-1.56803	-4.54151	1.31048
H	-3.45842	2.55552	2.37380
H	-3.21980	-2.70748	2.34032
C	0.21830	3.48660	-0.28938
C	0.63522	-3.35580	-0.03442
C	-2.43558	-0.05108	1.71195
C	3.46839	0.19651	-1.74536
H	0.14824	4.56759	-0.37061
H	0.73835	-4.42943	0.10071
H	-3.27179	-0.10002	2.40451
H	4.42163	0.25400	-2.26283
C	1.24745	0.99492	2.78319
C	2.37051	-0.80173	2.32909
C	2.75897	-0.41066	3.58172
N	1.42477	0.08131	1.83869
N	2.03533	0.73332	3.85184
H	3.46209	-0.82697	4.28588
H	2.70074	-1.64680	1.74662
H	0.57661	1.83688	2.72390
H	2.08436	1.28660	4.69619
C	-0.94941	-0.73653	-1.10379
C	-2.17004	0.08762	-1.47395
O	-2.11144	1.09585	-2.15176
O	-3.33809	-0.50572	-1.15002
C	-4.54318	0.19039	-1.55024
H	-4.53290	0.31428	-2.63750
H	-4.53599	1.18664	-1.09713
C	-5.72558	-0.63815	-1.08394
H	-6.65945	-0.14328	-1.37193
H	-5.70970	-1.63425	-1.53830
H	-5.71783	-0.75354	0.00471
C	-0.71794	-1.62737	-2.32878
H	-0.68888	-0.97582	-3.20760
H	0.21266	-2.18552	-2.30008
H	-1.55050	-2.33362	-2.46032

(Fe,N)-bridged IPC 1 triplet

Fe	0.54219400	0.17366300	-0.18314500
N	1.91645500	1.57165900	-0.70333800
N	1.67305200	-1.28717000	-0.90755100
N	-0.64995000	1.53723500	0.60782100
N	-1.33001500	-1.48059900	0.02597300
C	1.78776100	2.92426700	-0.54543800
C	1.44232400	-2.64926900	-0.84115600
C	3.08426600	1.35384800	-1.38099900
C	2.91839000	-1.13192400	-1.47780600
C	-0.39768300	2.89017000	0.65699200
C	-0.87145200	-2.78659300	0.18934500
C	-1.84001500	1.33545500	1.28131400
C	-2.15856200	-1.16991000	1.10145600
C	2.92223900	3.59366800	-1.14273500
C	2.59058300	-3.36318800	-1.37187200
C	3.72832800	2.61825800	-1.66125000
C	3.49037200	-2.42971700	-1.78173900
C	-1.45620500	3.56360800	1.38309700
C	-1.64272800	-3.37636900	1.24777500
C	-2.33489700	2.60541100	1.78314300
C	-2.42100800	-2.39335300	1.80281300
H	3.07426000	4.66597700	-1.16313300
H	2.66656000	-4.44189300	-1.43522100
H	4.66677700	2.73760400	-2.18879700
H	4.45899500	-2.58510300	-2.24048900
H	-1.50062400	4.63138700	1.55891900
H	-1.50488700	-4.38906700	1.60400700
H	-3.25061200	2.72773900	2.34868500
H	-3.03987600	-2.46232500	2.68805600
C	0.71598500	3.53372200	0.11579000
C	0.31724300	-3.31168700	-0.32879200
C	-2.48282600	0.11643800	1.54081200
C	3.56233800	0.08272000	-1.71690900
H	0.74801200	4.61532800	0.21561600
H	0.43060100	-4.38716300	-0.21335300
H	-3.29377600	0.16648100	2.26361400
H	4.52879400	0.03212800	-2.21111900

C	0.96439900	0.30582100	2.98469100
C	2.27593400	-1.23285500	2.21995800
C	2.54894800	-1.12775900	3.55750800
N	1.28336400	-0.33529100	1.87035500
N	1.70343000	-0.14309000	4.02777100
H	3.24460600	-1.64397100	4.20049600
H	2.72169900	-1.88635800	1.48687800
H	0.22245000	1.08374000	3.07230600
H	1.64671300	0.19216200	4.97947800
C	-1.07821600	-0.63027800	-1.15315400
C	-2.22655500	0.29724100	-1.50691300
O	-2.08503300	1.33704600	-2.12647800
O	-3.45514400	-0.21163600	-1.23953800
C	-4.58314100	0.60449100	-1.62326700
H	-4.54334400	0.78087200	-2.70284900
H	-4.50131600	1.57511400	-1.12319700
C	-5.84411200	-0.13657800	-1.21737500
H	-6.72575800	0.45168300	-1.49464700
H	-5.90642500	-1.10753700	-1.71980300
H	-5.86786300	-0.30534600	-0.13574900
C	-0.92981100	-1.43384600	-2.46477500
H	-0.88057400	-0.71640800	-3.28900500
H	-0.03461200	-2.04666600	-2.51835700
H	-1.80243700	-2.08459000	-2.63200900

(Fe,N)-bridged IPC 1 quintet

Fe	0.53398	0.19921	-0.13328
N	1.67833	1.80431	-0.66159
N	1.95303	-1.13526	-0.88157
N	-0.96357	1.44777	0.61405
N	-1.09568	-1.64619	-0.10938
C	1.34176	3.12117	-0.49833
C	1.89513	-2.50218	-0.89180
C	2.90682	1.74949	-1.26210
C	3.16574	-0.76235	-1.39485
C	-0.89244	2.81460	0.64350
C	-0.43920	-2.87879	0.07121
C	-2.12131	1.07371	1.23862
C	-1.97327	-1.45600	0.97514
C	2.41029	3.94879	-1.02910
C	3.14234	-3.02794	-1.41524
C	3.37594	3.10331	-1.49841
C	3.92518	-1.95241	-1.73307
C	-2.06283	3.33608	1.32358
C	-1.14493	-3.57540	1.11797
C	-2.81641	2.25825	1.70371
C	-2.05785	-2.71833	1.66289
H	2.41578	5.03205	-1.03716
H	3.37747	-4.07879	-1.53457
H	4.31919	3.36547	-1.96221
H	4.91816	-1.95874	-2.16610
H	-2.27929	4.38586	1.48090
H	-0.86734	-4.55787	1.47740
H	-3.76017	2.26315	2.23601
H	-2.66888	-2.88004	2.54166
C	0.16463	3.57933	0.11536
C	0.81429	-3.27464	-0.41359
C	-2.51980	-0.26200	1.45612
C	3.59558	0.56576	-1.57495
H	0.05884	4.65823	0.19818
H	1.02651	-4.33368	-0.28202
H	-3.32278	-0.39775	2.17768
H	4.57862	0.69026	-2.02229
C	0.82421	0.40517	3.07791
C	2.27420	-1.04870	2.39767
C	2.46712	-0.91751	3.74703
N	1.24484	-0.22081	1.98914
N	1.53460	0.01206	4.16233
H	3.15867	-1.38323	4.43162
H	2.79839	-1.67491	1.69260
H	0.02753	1.13181	3.11544
H	1.40585	0.34813	5.10684
C	-0.98498	-0.81934	-1.31455
C	-2.18418	-0.01237	-1.70090
O	-2.12145	0.94206	-2.46323
O	-3.37633	-0.48407	-1.25745
C	-4.54229	0.28734	-1.61790
H	-4.59700	0.36135	-2.70828
H	-4.43079	1.30094	-1.21900
C	-5.75596	-0.41724	-1.03912
H	-6.66515	0.13602	-1.29923
H	-5.84584	-1.43318	-1.43798
H	-5.69007	-0.47934	0.05205
C	-0.60069	-1.59237	-2.58423
H	-0.75902	-0.92597	-3.43549
H	0.43639	-1.91841	-2.61914
H	-1.23959	-2.48050	-2.72252

QM/MM optimized structures (only QM-region atoms):

IPC 1 Rma TDE closed-shell singlet (QM-region atoms only)

C	39.499402	28.967232	30.655753
C	38.635442	29.044470	31.712278
N	39.361884	27.686363	30.151462
C	38.416891	27.054985	30.897981
N	37.965431	27.850746	31.846483
H	39.821352	27.304008	29.329581
H	38.445929	29.872439	32.379099
H	38.072922	26.052034	30.704353
Fe	36.282989	27.421716	33.179508
C	34.195300	24.023195	29.153469
C	37.830592	21.956282	32.664369
N	35.342721	26.710408	31.538300
C	34.956213	23.939626	27.822010
C	36.925084	20.997916	33.486356
N	35.616495	29.314226	32.755026
C	34.419419	22.788407	26.911481
C	37.337994	20.939903	34.989272
N	37.144853	25.600879	33.431167
C	36.017718	24.350943	31.666095
C	34.347702	28.794916	30.720282
C	36.632465	30.514537	34.622277
C	38.721798	26.187722	35.207359
C	35.304765	25.408040	31.104622
C	34.857759	29.674985	31.677727
C	37.390099	29.469567	35.151369
C	38.187657	25.316240	34.270786
O	35.179374	22.441314	25.974991
O	36.612545	21.624100	35.781231
C	34.458608	25.279590	29.920923
C	34.609931	31.097515	31.690425
C	38.347647	29.619236	36.227470
C	38.644691	23.957586	34.078407
O	33.273339	22.347075	27.180662
O	38.351884	20.274940	35.286172
C	33.994617	26.542027	29.664520
C	35.214089	31.597807	32.817911
C	38.931094	28.392261	36.412159
C	37.829756	23.383066	33.146871
C	34.554032	27.420876	30.664430
C	35.845161	30.463473	33.471175
C	38.337193	27.508598	35.426603
C	36.914121	24.447742	32.725872
N	37.407431	28.182361	34.681804
H	35.880789	21.318142	33.395993
H	37.019902	19.998215	33.041851
H	34.838058	24.883309	27.269757
H	36.031329	23.803200	27.970768
H	37.532609	21.916581	31.608520
H	38.851877	21.564501	32.710086
H	34.425746	23.140870	29.760463
H	33.135255	23.919207	28.897664
H	39.488964	25.773469	35.848019

H	36.712292	31.466685	35.135539
H	33.725755	29.230622	29.943177
H	35.909285	23.380329	31.197258
C	34.845160	27.052959	34.238425
C	34.833852	25.883156	35.158173
O	35.303312	25.879533	36.288157
O	34.183369	24.861022	34.588931
C	34.118047	23.576581	35.272390
C	33.154126	22.731290	34.461444
C	33.546444	27.812125	34.235861
H	33.777705	23.741730	36.299561
H	35.112929	23.117642	35.307647
H	33.439282	22.751100	33.404793
H	33.199132	21.691756	34.796019
H	32.121360	23.091900	34.545378
H	33.185206	27.946930	33.209628
H	32.757802	27.323814	34.824573
H	33.706777	28.821924	34.636147
O	37.416051	23.837412	37.154098
H	37.185273	23.005725	36.674758
H	36.739489	24.473523	36.873184

IPC 1 Rma TDE open-shell singlet (QM-region atoms only)

C	39.499402	28.967232	30.655753
C	38.635442	29.044470	31.712278
N	39.361884	27.686363	30.151462
C	38.416891	27.054985	30.897981
N	37.965431	27.850746	31.846483
H	39.821352	27.304008	29.329581
H	38.445929	29.872439	32.379099
H	38.072922	26.052034	30.704353
Fe	36.282989	27.421716	33.179508
C	34.195300	24.023195	29.153469
C	37.830592	21.956282	32.664369
N	35.342721	26.710408	31.538300
C	34.956213	23.939626	27.822010
C	36.925084	20.997916	33.486356
N	35.616495	29.314226	32.755026
C	34.419419	22.788407	26.911481
C	37.337994	20.939903	34.989272
N	37.144853	25.600879	33.431167
C	36.017718	24.350943	31.666095
C	34.347702	28.794916	30.720282
C	36.632465	30.514537	34.622277
C	38.721798	26.187722	35.207359
C	35.304765	25.408040	31.104622
C	34.857759	29.674985	31.677727
C	37.390099	29.469567	35.151369
C	38.187657	25.316240	34.270786
O	35.179374	22.441314	25.974991
O	36.612545	21.624100	35.781231
C	34.458608	25.279590	29.920923
C	34.609931	31.097515	31.690425
C	38.347647	29.619236	36.227470
C	38.644691	23.957586	34.078407
O	33.273339	22.347075	27.180662
O	38.351884	20.274940	35.286172
C	33.994617	26.542027	29.664520
C	35.214089	31.597807	32.817911
C	38.931094	28.392261	36.412159
C	37.829756	23.383066	33.146871
C	34.554032	27.420876	30.664430
C	35.845161	30.463473	33.471175
C	38.337193	27.508598	35.426603
C	36.914121	24.447742	32.725872
N	37.407431	28.182361	34.681804
H	35.880789	21.318142	33.395993
H	37.019902	19.998215	33.041851
H	34.838058	24.883309	27.269757
H	36.031329	23.803200	27.970768
H	37.532609	21.916581	31.608520
H	38.851877	21.564501	32.710086
H	34.425746	23.140870	29.760463
H	33.135255	23.919207	28.897664
H	39.488964	25.773469	35.848019
H	36.712292	31.466685	35.135539
H	33.725755	29.230622	29.943177
H	35.909285	23.380329	31.197258
C	34.845160	27.052959	34.238425
C	34.833852	25.883156	35.158173
O	35.303312	25.879533	36.288157
O	34.183369	24.861022	34.588931
C	34.118047	23.576581	35.272390
C	33.154126	22.731290	34.461444
C	33.546444	27.812125	34.235861
H	33.777705	23.741730	36.299561
H	35.112929	23.117642	35.307647
H	33.439282	22.751100	33.404793
H	33.199132	21.691756	34.796019
H	32.121360	23.091900	34.545378
H	33.185206	27.946930	33.209628
H	32.757802	27.323814	34.824573
H	33.706777	28.821924	34.636147
O	37.416051	23.837412	37.154098
H	37.185273	23.005725	36.674758
H	36.739489	24.473523	36.873184

IPC 1 Rma TDE triplet singlet (QM-region atoms only)

C	39.524928	28.965513	30.644307
C	38.673898	29.040292	31.710286
N	39.368927	27.691750	30.126769
C	38.424738	27.061606	30.872816
N	37.993038	27.852192	31.835034
H	39.821880	27.311949	29.299956
H	38.498252	29.862171	32.388254
H	38.068554	26.063871	30.673139
Fe	36.332516	27.436669	33.191865
C	34.188407	24.013735	29.189708
C	37.833091	21.976333	32.687114
N	35.332657	26.693714	31.589232
C	34.966441	23.934237	27.867277
C	36.922112	21.015483	33.498242
N	35.675355	29.316275	32.773414
C	34.427033	22.800594	26.934979
C	37.341575	20.941536	34.999291
N	37.159974	25.624902	33.441053
C	36.004695	24.341731	31.708825
C	34.377228	28.784301	30.750261
C	36.675641	30.534017	34.643120
C	38.738562	26.205860	35.228466
C	35.286767	25.394327	31.151428
C	34.898068	29.664659	31.702011
C	37.427220	29.490246	35.177617
C	38.200344	25.340469	34.288852
O	35.194637	22.455304	26.004040
O	36.614055	21.607934	35.801302
C	34.445193	25.267904	29.963535
C	34.641695	31.082207	31.713788
C	38.382119	29.635909	36.256607
C	38.649557	23.981463	34.101720
O	33.272150	22.371477	27.183918
O	38.365519	20.282777	35.279154
C	33.994460	26.533302	29.704140
C	35.246946	31.591600	32.838670
C	38.959849	28.406723	36.439529
C	37.829222	23.401835	33.174494
C	34.560138	27.408508	30.706058
C	35.891859	30.470630	33.491470
C	38.361318	27.527586	35.451521
C	36.915780	24.458872	32.751872
N	37.438973	28.205627	34.706428
H	35.879808	21.343356	33.414848
H	37.011004	20.020376	33.042181
H	34.867487	24.885370	27.324175

H	36.037269	23.781748	28.028807
H	37.544356	21.943539	31.628396
H	38.853669	21.583677	32.739690
H	34.409251	23.129416	29.797592
H	33.132292	23.912438	28.917363
H	39.496352	25.781478	35.873051
H	36.748825	31.488104	35.153171
H	33.756843	29.223157	29.974210
H	35.891410	23.364700	31.255517
C	34.809997	27.122655	34.383061
C	34.824151	25.916041	35.226489
O	35.418276	25.793884	36.292825
O	34.058988	24.934408	34.693457
C	34.055668	23.630029	35.326790
C	33.110382	22.773246	34.504273
C	33.472289	27.763237	34.143030
H	33.729546	23.736087	36.367004
H	35.064897	23.204145	35.336319
H	33.384269	22.826952	33.445604
H	33.186870	21.727390	34.813160
H	32.068559	23.102633	34.604677
H	33.148758	27.695662	33.096089
H	32.687405	27.305434	34.762205
H	33.507866	28.836358	34.378676
O	37.474920	23.816569	37.152263
H	37.220864	22.981589	36.692069
H	36.791124	24.451163	36.881617

IV. Supplementary references

1. Gibson DG, *et al.* (2009) Enzymatic assembly of DNA molecules up to several hundred kilobases. *Nat Methods* 6:343–345.

2. Arslan E, Schulz H, Zufferey R, Kunzler P, Thony-Meyer L (1998) Overproduction of the *Bradyrhizobium japonicum c*-type cytochrome subunits of the cbb(3) oxidase in *Escherichia coli*. *Biochem Biophys Res Commun* 251(3):744–747.

3. Sambrook J, Russell DW (2001) Molecular Cloning: A Laboratory Manual. *Cold Spring Harb Lab Press. Cold Spring Harb. NY* 999. doi:10.1016/0092-8674(90)90210-6

4. Kan SBJ, Lewis RD, Chen K, Arnold FH (2016) Directed evolution of cytochrome *c* for carbon–silicon bond formation: Bringing silicon to life. *Science* 354(6315):1048–1051.

5. Liptak MD, Wen X, Bren KL (2010) NMR and DFT investigation of heme ruffling: Functional implications for cytochrome *c*. *J Am Chem Soc* 132(28):9753–9763.

6. Berry EA, Trumpower BL (1987) Simultaneous determination of hemes *a*, *b*, and *c* from pyridine hemochrome spectra. *Anal Biochem* 161(1):1–15.

7. Stelter M, Melo AM, Saraiva LM, Teixeira M, Archer M (2007) Crystallization and X-ray analysis of *Rhodothermus marinus* cytochrome *c* at 1.23 A resolution. *Protein Pept Lett* 14(10):1038–1040.

8. Kabsch W (2010) XDS. *Acta Cryst D* 66(Pt 2):125–132.

9. Evans PR, Murshudov GN (2013) How good are my data and what is the resolution? *Acta Cryst D* 69(Pt 7):1204–1214.

10. McCoy AJ, Grosse-Kunstleve RW, Adams PD, Winn MD, Storoni LC, Read RJ (2007) *Phaser* crystallographic software. *J Appl Cryst* 40(Pt 4):658-674.

11. Winn MD, *et al.* (2011) Overview of the CCP4 suite and current developments. *Acta Cryst D* 67(Pt 4):235-242.

12. Stelter M, *et al.* (2008) A novel type of monoheme cytochrome *c*: Biochemical and structural characterization at 1.23 Å resolution of *Rhodothermus marinus* cytochrome *c*. *Biochemistry* 47(46):11953–11963.

13. Winn MD, Murshudov GN, Papiz MZ (2003) Macromolecular TLS refinement in REFMAC at moderate resolutions. *Methods Enzymol* 374:300–321.

14. Emsley P, Cowtan K (2004) *Coot:* model-building tools for molecular graphics. *Acta Cryst D* 60(Pt 12 Pt 1):2126–2132.

15. Chen VB, Arendall III WB, Headd JJ, Keedy DA, Immormino RM, Kapral GJ, Murray LW, Richardson JS, Richardson DC (2010) *MolProbity:* all-atom structure validation for macromolecular crystallography. *Acta Cryst D* 66(Pt 1):12–21.

16. Painter J, Merritt EA (2006) *TLSMD* web server for the generation of multi-group TLS models. *J Appl Cryst* 39(Pt 8):109–111.

17. Frisch MJ, *et al.* (2009) Gaussian 09, Revision A. 02. Gaussian. Inc.*: Wallingford, CT*.

18. Becke AD (1988) Density-functional exchange-energy approximation with correct asymptotic behavior. *Phys Rev A* 38(6):3098–3100.

19. Becke AD (1993) Density‐functional thermochemistry. III. The role of exact exchange. *J Chem Phys* 98(7):5648–5652.

20. Lee C, Yang W, Parr RG (1988) Development of the Colle-Salvetti correlation-energy formula into a functional of the electron density. *Phys Rev B* 37(2):785–789.

21. Ribeiro RF, Marenich AV, Cramer CJ, Truhlar DG (2011) Use of solution-phase vibrational frequencies in continuum models for the free energy of solvation. *J Phys Chem B* 115(49):14556–14562.

22. Zhao Y, Truhlar DG (2008) Computational characterization and modeling of buckyball tweezers: density functional study of concave-convex pi…pi interactions. *Phys Chem Chem Phys* 10(19):2813–2818.

23. Funes-Ardoiz I, Paton RS (2016) GoodVibes: GoodVibes v1.0.1. doi:10.5281/zenodo.60811

24. Grimme S, Ehrlich S, Goerigk L (2011) Effect of the damping function in dispersion corrected density functional theory. *J Comput Chem* 32(7):1456-1465.

25. Grimme S, Antony J, Ehrlich S, Krieg H (2010) A consistent and accurate *ab initio* parametrization of density functional dispersion correction (DFT-D) for the 94 elements H-Pu. *J Chem Phys* 132(15):154104.

26. Barone V, Cossi M (1998) Quantum calculation of molecular energies and energy gradients in solution by a conductor solvent model. *J Phys Chem A* 102(11):1995–2001.

27. Cossi M, Rega N, Scalmani G, Barone V (2003) Energies, structures, and electronic properties of molecules in solution with the C-PCM solvation model. *J Comput Chem* 24(6):669–681.

28. Schutz CN, Warshel A (2001) What are the dielectric “constants” of proteins and how to validate electrostatic models? *Proteins* 44(4):400–417.

29. Li L, Li C, Zhang Z, Alexov E (2013) On the dielectric “constant” of proteins: Smooth dielectric function for macromolecular modeling and its implementation in DelPhi. *J Chem Theory Comput* 9(4):2126–2136.

30. Sharon DA, Mallick D, Wang B, Shaik S (2016) Computation sheds insight into iron porphyrin carbenes’ electronic structure, formation, and N–H insertion reactivity. *J Am Chem Soc* 138(30):9597–9610.

31. Postils V, *et al.* (2018) The mechanism of the selective Fe-catalyzed arene carbon–hydrogen bond functionalization. *ACS Catal* 8:4313–4322.

32. Narayan ARH, *et al.* (2015) Enzymatic hydroxylation of an unactivated methylene C–H bond guided by molecular dynamics simulations. *Nature Chemistry* 7(8):653–660.

33. Gilbert MM, *et al.* (2017) Synthesis of diverse 11- and 12-membered macrolactones from a common linear substrate using a single biocatalyst. *ACS Cent Sci* 3(12):1304–1310.

34. Shaik S, *et al.* (2010) P450 Enzymes: Their structure, reactivity, and selectivity–modeled by QM/MM calculations. *Chem Rev* 110(2):949-1017.

35. Chen H, Lai W, Shaik S (2010) Exchange-enhanced H-abstraction reactivity of high-valent nonheme iron(IV)-oxo from coupled cluster and density functional theories. *J Phys Chem Lett* 1(10):1533–1540.

36. Altun A, Breidung J, Neese F, Thiel W (2014) Correlated *ab initio* and density functional studies on H2 activation by FeO+. *J Chem Theory Comput* 10(9):3807–3820.

37. Seeger R, Pople JA (1977) Self-consistent molecular orbital methods. XVIII. Constraints and stability in Hartree–Fock theory. *J Chem Phys* 66(7)3045–3050.

38. Bauernschmitt R, Ahlrichs R (1996) Stability analysis for solutions of the closed shell Kohn–Sham equation. *J Chem Phys* 104(22):9047–9052.

39. Schlegel HB, McDouall JJW (1991) Computational Advances in Organic Chemistry: Molecular Structure and Reactivity, eds Ögretir C, Csizmadia IG (Springer Netherlands) pp. 167–185.

40. Legault C. (2009) CYLview, 1.0 b, Université de Sherbrooke, Sherbrooke, Québec, Canada. *URL* http://www.cylview.org

41. Dapprich S, Komáromi I, Byun KS, Morokuma K, Frisch MJ (1999) A new ONIOM implementation in Gaussian98. Part I. The calculation of energies, gradients, vibrational frequencies and electric field derivatives. *Journal of Molecular Structure: THEOCHEM* 461-462:1–21.

42. Chung LW, *et al.* (2015) The ONIOM method and its applications. *Chem Rev* 115(12):5678–5796.

43. Vreven T, *et al.* (2006) Combining quantum mechanics methods with molecular mechanics methods in ONIOM. *J Chem Theory Comput* 2(3):815–826.

44. Tao P, Schlegel HB (2010) A toolkit to assist ONIOM calculations. *J Comput Chem* 31(12):2363–2369.

45. Neese F, Petrenko T (2011) Mössbauer Spectroscopy and Transition Metal Chemistry: Fundamentals and Applications (Springer Berlin Heidelberg) pp 137–199.

46. Römelt M, Ye S, Neese F (2009) Calibration of modern density functional theory methods for the prediction of 57Fe Mössbauer isomer shifts: Meta-GGA and double-hybrid functionals. *Inorg Chem* 48(3):784–785.

47. Neese F (2012) The ORCA program system. *Wiley Interdiscip Rev: Comput Mol Sci* 2(1):73–78.

48. Tao J, Perdew JP, Staroverov VN, Scuseria GE (2003) Climbing the density functional ladder: Nonempirical meta–generalized gradient approximation designed for molecules and solids. *Phys Rev Lett* 91()14:146401.

49. Bjornsson R, Neese F, DeBeer S (2017) Revisiting the Mössbauer isomer shifts of the FeMoco cluster of nitrogenase and the cofactor charge. *Inorg Chem* 56(3):1470–1477.

50. Salomon-Ferrer R, Götz AW, Poole D, Le Grand S, Walker RC (2013) Routine microsecond molecular dynamics simulations with AMBER on GPUs. 2. Explicit solvent particle mesh ewald. *J Chem Theory Comput* 9(9):3878-3888.

51. AMBER 2017 (University of California, San Francisco, 2017).

52. Li P, Merz KM (2016) MCPB.py: A Python based metal center parameter builder. *J. Chem. Inf. Model.* 56(4):599–604.

53. Wang J, Wolf RM, Caldwell JW, Kollman PA, Case DA (2004) Development and testing of a general amber force field. *J Comput Chem* 25(9):1157–1174.

54. Bayly CI, Cieplak P, Cornell W, Kollman PA (1993) A well-behaved electrostatic potential based method using charge restraints for deriving atomic charges: the RESP model. *J Phys Chem* 97(40):10269–10280.

55. Besler BH, Merz KM, Kollman PA (1990) Atomic charges derived from semiempirical methods. *J Comput Chem* 11(4):431–439.

56. Singh UC, Kollman PA (1984) An approach to computing electrostatic charges for molecules. *J Comput Chem* 5(2):129–145.

57. Jorgensen WL, Chandrasekhar J, Madura JD, Impey RW, Klein ML (1983) Comparison of simple potential functions for simulating liquid water. *J Chem Phys* 79(2):926–935.

58. Maier JA, *et al.* (2015) ff14SB: Improving the Accuracy of Protein Side Chain and Backbone Parameters from ff99SB. *J Chem Theory Comput* 11(8):3696–3713.

59. Darden T, York D, Pedersen L (1993) Particle mesh Ewald: An N $\cdot$ log(N) method for Ewald sums in large systems. *J Chem Phys* 98(12):10089–10092.

60. Roe DR, Cheatham TE (2013) PTRAJ and CPPTRAJ: Software for processing and analysis of Molecular Dynamics trajectory data. *J Chem Theory Comput* 9(7):3084–3095.

61. Li Y, Huang J, Zhou Z, Che C, You X (2002) Remarkably stable iron porphyrins bearing nonheteroatom-stabilized carbene or (alkoxycarbonyl)carbenes: Isolation, X-ray crystal structures, and carbon atom transfer reactions with hydrocarbons. *J Am Chem Soc* 124(44):13185–13193.

62. English DR, Hendrickson DN, Suslick KS (1983) Mössbauer spectra of oxidized iron porphyrins. *Inorg Chem* 22(2):367–368.

63. Khade RL, *et al.* (2014) Iron porphyrin carbenes as catalytic intermediates: Structures, Mössbauer and NMR spectroscopic properties, and bonding. *Angew Chem Int Ed* 53(29):7574–7578.

64. Stone KL, Hoffart LM, Behan RK, Krebs C, Green MT (2006) Evidence for two ferryl species in chloroperoxidase compound II. *J Am Chem Soc* 128(18):6147–6153.

65. Behan RK, Hoffart LM, Stone KL, Krebs C, Green MT (2006) Evidence for basic ferryls in cytochromes P450. *J Am Chem Soc* 128(35):11471–11474.

66. Yosca TH, Rittle J, Krest CM, Onderko EL, Silakov A, Calixto JC, Behan RK, Green MT (2013) Iron(IV)hydroxide pK(a) and the role of thiolate ligation in C-H bond activation by cytochrome P450. *Science* 342(6160):825–829.

67. Jentzen W, Song XZ, Shelnutt JA (1997) Structural characterization of synthetic and protein-bound porphyrins in terms of the lowest-frequency normal coordinates of the macrocycle. *J Phys Chem B* 101(9):1684–1699.

68. Graves AB, Graves MT, Liptak MD (2016) Measurement of heme ruffling changes in MhuD using UV–Vis spectroscopy. *J Phys Chem B* 120(16):3844–3853.

69. Chen D, Zhu DX, Xu MH (2016) Rhodium(I)-catalyzed highly enantioselective insertion of carbenoid into Si–H: Efficient access to functional chiral silanes. *J Am Chem Soc* 138(5):1498–1501.